Novel Nanocomposite Membrane Structures for H$_2$ Separations

Final Technical Progress Report

Reporting Period:
August 27, 2001 – March 31, 2005

Principal Author:
Benny D. Freeman

Department of Chemical Engineering
The University of Texas at Austin
Austin, TX 78758

Date Issued: March 31, 2005

DISCLAIMER

This report was prepared as an account of work sponsored by an agency of the United States Government. Neither the United States Government nor any agency thereof, nor any of their employees, makes any warranty, express or implied, or assumes any legal liability or responsibility for the accuracy, completeness, or usefulness of any information, apparatus, product, or process disclosed, or represents that its use would not infringe on privately owned rights. Reference herein to any specific commercial product, process, or service by trade name, trademark, manufacture, or otherwise does not necessarily constitute or imply its endorsement, recommendation, or favoring by the United States Government or any agency thereof. The views and opinions of authors expressed herein do not necessarily state or reflect those of the United States Government or any agency thereof.

Table of Contents

.

Abstract

This report explores possible methods of improving CO_2 selectivity in polymer based membranes. The first method investigated using basic nanoparticles to enhance the solubility of acid gases in nanocomposite membranes, thus enhancing the overall acid gas/light gas selectivity (*e.g.*, CO_2/H_2, CO_2/CH_4, *etc.*). The influence of nanoparticle surface chemistry on nanocomposite morphology and transport properties will be determined experimentally in a series of poly(1-trimethylsilyl-1-propyne). Additional factors (*e.g.*, chemical reaction of the particles with the polymers) have been considered, as necessary, during the course of the investigation. The second method investigated using polar polymers such as crosslinked poly(ethylene oxide) and poly(ether-b-amide) to improve CO_2 sorption and thereby increase CO_2 permeability and CO_2/light gas selectivity. For both types of materials, CO_2 and light gas permeabilities have been characterized. The overall objective was to improve the understanding of materials design strategies to improve acid gas transport properties of membranes.

1. Introduction

There is a significant need for economical, environmentally benign methods of removing acid gases from mixtures with light gases. Numerous industrially important gas separations require the removal of acid gases from light gases. Such separations include CO_2 removal from natural gas[1] and from steam-reformed H_2.[2] Many times, these and other separations require the removal of acid gases such as H_2S and SO_2 in addition to CO_2.

There are many disadvantages to current acid gas removal technologies. Amine scrubbing columns [ASC], physical solvent processes [PSP], and pressure-swing adsorption [PSA] are generally used to remove acid gases from valuable product gas streams.[2] Each of these technologies has significant drawbacks, such as high capital cost, complexity of operation, and large space requirements.[2] ASC and PSP use solvents which must be regenerated by heat or pressure, thus increasing process complexity.[2] ASC solvents include monoethanolamine, diethanolamine, and methyldiethanolanime, all of which are corrosive, environmentally hazardous, and subject to chemical degradation.[3] Membranes may represent an alternative method of acid gas removal without many of the difficulties associated with conventional acid gas separation techniques. Membranes have a small footprint, low capital cost, are easy to install and operate and have little environmental impact.[2] However, the current use of membranes in industry is often limited by their permeability and selectivity.

This research project focuses primarily on the materials science related to improving membranes for CO_2 removal from H_2-rich streams. Efficiently removing acid gases from steam reformer product streams is a key goal in moving towards the H_2 economy.[4] Steam reforming of hydrocarbons and the subsequent water gas shift reaction is the major route for producing hydrogen:[5]

$$C_xH_y + xH_2O \rightleftharpoons xCO + (y/2+x)H_2 \tag{1}$$

$$CO + H_2O \rightleftharpoons CO_2 + H_2 \tag{2}$$

This process produces a large number of by-products, such as CO_2, that must be removed from the H_2 rich stream.

CO_2/H_2 selectivity and CO_2 permeability should be maximized to reduce system H_2 loss and H_2 pressure loss. By removing CO_2 from H_2 (rather than the technologically simpler removal of H_2 from CO_2), expensive downstream pressurization of H_2 for later use in petrochemical processing or fuel cells is eliminated. Such reverse-selective membranes could reduce overall system costs (*i.e.*, capital equipment, energy, and raw material costs) relative to those obtained with conventional H_2-selective membranes.

Permeability selectivity depends on both diffusivity selectivity and solubility selectivity.[6] Diffusivity selectivity depends on the size-sieving ability of a polymer. In separations involving CO_2 and H_2, diffusivity selectivity will favor H_2 since it has a smaller kinetic diameter (2.8 Å) than CO_2 (3.3 Å).[7] The kinetic diameter is the minimum zeolite pore size diameter that allows a gas molecule to access the pore.[7] Solubility selectivity depends on penetrant condensability and polymer-penetrant interactions. For CO_2/H_2 separations, CO_2 is far more soluble than H_2 based on the much higher condensability (as measured by critical temperature, for example) of CO_2.[8] Therefore, solubility selectivity will favor CO_2 over H_2. CO_2/H_2 permselective membranes must minimize the effect of diffusivity selectivity while maximizing solubility selectivity. High free volume polymers (*e.g.,* poly(1-trimethylsilyl-1-propyne) [PTMSP]) have low enough diffusivity selectivity to be more permeable to CO_2 than to H_2.[9] Polymers with a CO_2/H_2 permselectivity > 1 are referred to as "reverse selective" since the larger penetrant has a higher permeability coefficient than the smaller gas.

One method of increasing penetrant gas permeability in a polymer is to increase diffusion coefficients. Addition of inert, impermeable, nanosized particles to high free volume, stiff-chained, glassy polymers can increase diffusion coefficients and, in turn, enhance gas permeability.[10]

Polymers can be designed to have favorable interactions with CO_2, thus enhancing its solubility. Since CO_2 is an acid gas, it is possible to increase the basicity of the membrane to enhance acid gas/light gas solubility selectivity. One method involves using polymers with polar moieties, such as ether groups, *e.g.*, poly(ethylene oxide) [PEO], and poly(ether-b-amide) [Pebax].[11,12] An alternative is to include particles which have an affinity towards CO_2. Many metals and metal oxides are basic and can adsorb

CO_2.[13] Certain metals oxides, such as MgO, adsorb as much as 10 wt. % CO_2 at room temperature and 20 Torr partial pressure.[14] Research conducted under this grant focused on polymers with polar moieties, and the addition of basic nanoparticles to polymeric matrices. Both materials attemped to increase solubility selectivity in favor of CO_2 as a route to increasing permeability selectivity. Polymer and nanocomposite gas transport properties, and, when applicable, polymer-particle dispersion and interaction, were characterized.

2. Background

Gas Transport in Polymers

The permeability of a gas A, P_A, through a film of thickness l is: [6]

$$P_A \equiv \frac{N_A l}{(p_2 - p_1)} \tag{3}$$

where N_A is the steady state gas flux through the film, and p_2 and p_1 are the feed and permeate partial pressures, respectively,

If Fick's law is obeyed, and the downstream pressure, p_1, is much lower than the upstream pressure, p_2, the permeability is often expressed as: [6]

$$P_A = S_A \times D_A \tag{4}$$

where D_A is the effective, concentration-averaged diffusivity. The solubility coefficient, S_A, is defined as C_2/p_2, where C_2 is the gas concentration in the polymer at the upstream face of the film. The ability of a polymer to separate two components is often characterized in terms of the ideal selectivity, $\alpha_{A/B}$, which is the ratio of permeabilities of the two components: [6]

$$\alpha_{A/B} \equiv \frac{P_A}{P_B} = \frac{D_A}{D_B} \times \frac{S_A}{S_B} \tag{5}$$

The ideal selectivity is, therefore, the product of D_A/D_B, the diffusivity selectivity, and S_A/S_B, the solubility selectivity. The diffusivity selectivity depends on the relative size of the penetrant molecules and the size-sieving ability of the polymer, which is largely a

function of free volume in the polymer matrix and polymer chain mobility.[15] Solubility selectivity is controlled by the relative condensability of the penetrants and the relative affinity of the penetrants for the polymer matrix.[15]

2.2 Gas Transport in Filled Polymeric Membranes

Adding impermeable particles to a polymer is typically expected to reduce membrane permeability.[16] Maxwell's model, which was developed to analyze steady state dielectric properties of a dilute suspension of spheres,[17] is often used to model permeability in membranes filled with roughly spherical impermeable particles:[18]

$$P_C = P_p \left(\frac{1 - \phi_f}{1 + \frac{\phi_f}{2}} \right) \qquad (6)$$

where P_c and P_p are the permeability of the composite and the pure polymer matrix, respectively. ϕ_f is the volume fraction of filler. The numerator represents the loss of membrane solubility due to the loss of polymer volume available for sorption.[19] The denominator represents a decrease in diffusivity due to increasing the penetrant diffusion pathway length.[19] Both factors act to decrease permeability with increasing particle volume fraction.[19]

Addition in fullerene particles (C_{60} and C_{70}) to poly(phenylene oxide) leads to a decrease of permeability without substantially changing membrane selectivity.[20] Chung *et al.* observed CO_2 permeability decrease from 7.2 Barrers[a] to 3.8 Barrers at 35 °C and 10 atm when 10 wt. % C_{60} was added to Matrimid 5218.[21] There was no change in CO_2/CH_4 selectivity.[21] In PTMSP, the addition of 5 wt. % fullerene substantially decreased permeability for all permanent gases and vapors considered.[22] For example, CO_2 permeability at 25 °C and 2 atm decreased from 27,000 Barrers to 7,000 Barrers.[22] Generally, the addition of fullerene particles to polymers decreases permeability in excess of the permeability loss predicted by Maxwell's model.

However, Higuchi *et al.* observed an increase in gas permeability upon adding fullerene particles to polystyrene.[23] Permeability increased 47% for N_2 and 75% for

---

[a] 1 Barrer = 10^{-10} cm^3(STP) cm/(cm^2 s cmHg)

ethane in a film containing 10 wt. % fullerene particles at 25 °C. Selectivity decreased about 25% for O_2/N_2 and ethylene/ethane. The enhancement in permeability was attributed to increases in diffusion coefficients caused by increased fractional free volume [FFV] in the membrane. In contrast, Maxwell's model predicts a 14 % loss in light gas permeability for this system.

Merkel *et al.* observed similar non-Maxwellian effects when adding very fine particles (12 nm primary particle diameter) to high free volume, rigid polymers.[10,24] Adding nanosized impermeable particles of commercial fumed silica [FS], TS-530, to a high free volume stiff chain glassy polymer (*e.g.*, poly(4-methyl-2-pentyne) [PMP]) increases gas and vapor permeabilities with increased particle loading (*cf.* Figure 2).[19] FS particles did not alter the solubility of the nanocomposite, but they did significantly increase gas diffusion coefficient (*cf.* Figures 3 and 4). For example, the CH_4 diffusion coefficient doubles when 30 wt. % FS is added to PMP at 25 °C.[19]
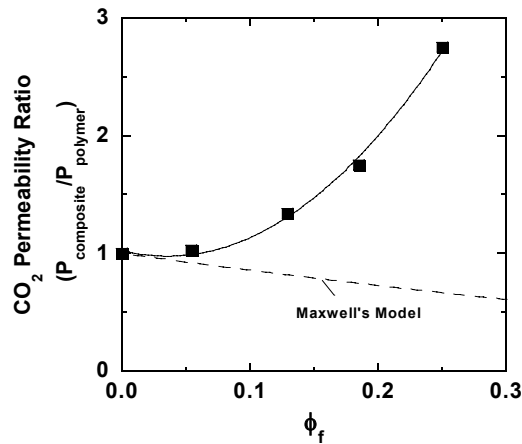
Figure 2. CO_2 permeability enhancement of PMP as a function of FS volume fraction in the composite membrane (■) at 25 °C and $\Delta P = 3.4$ atm.[19] The dashed line is the prediction of Maxwell's model (Eq. 6).
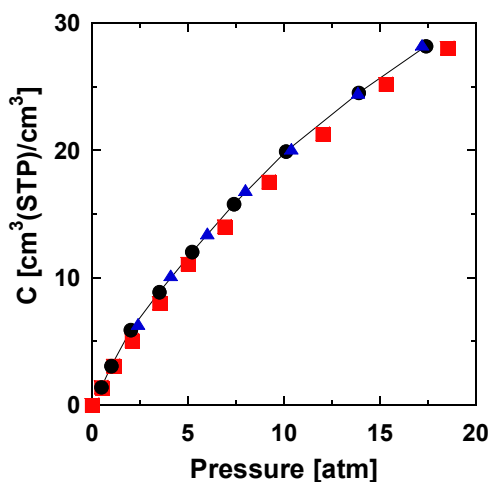
Figure 3. Concentration of CH_4 in PMP with increasing FS loading at 25 ^{o}C (▲) 0 wt. %, (●) 15 wt. %, and (■) 30 wt. %[19]
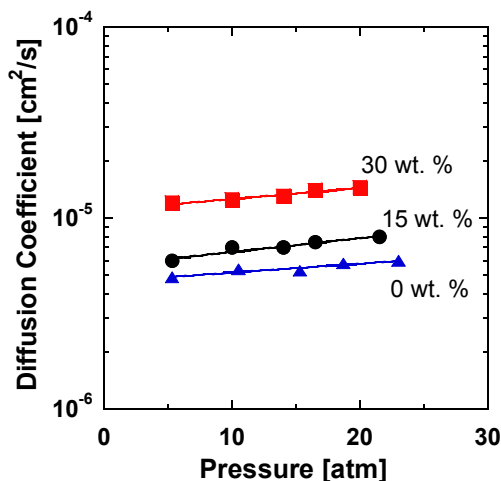
Figure 4. CH_4 diffusion coefficient in PMP with increasing FS loading at 25 ^{o}C(▲) 0 wt. %, (●) 15 wt. %, and (■) 30 wt. %[19]

The FS particles used in these studies were small enough (12 nm primary particle size) to disrupt polymer chain packing in the glassy, stiff-chain, high free volume polymers, which resulted in an increase in polymer fractional free volume.[24] The free volume increase was characterized using density and positron annihilation lifetime spectroscopy measurements. By increasing fractional free volume, gas diffusion coefficients and, in turn, gas permeability increase.[6]

Particle loading influences the gas transport properties in such nanocomposites. For examples, N_2 permeability triples as FS loadings in PMP increases from 5 vol. % to 25 vol. %.[25] With *n*-butane, enhancement in permeability coincided with a substantial enhancement in *n*-butane/CH_4 mixed gas selectivity.[25] Both *n*-butane permeability and *n*-butane/CH_4 selectivity enhancement have been attributed to increases in the FFV of PMP as FS particle loading increases.[25]

Barsema *et al*. used nanoparticles that selectively adsorb a permanent gas in an attempt to improve overall membrane selectivity.[26] Silver nanoparticles were incorporated into carbon molecular sieves [CMS] to increase O_2 permeability and O_2/N_2 selectivity. O_2 permeability increased from 16.8 to 81.3 Barrer in CMS pyrolyzed at 700 ^{o}C when Ag nanoparticles were included in the film.[26] For the same system, O_2/N_2
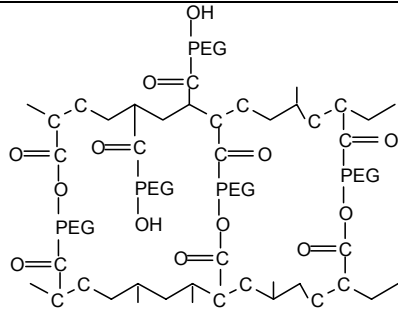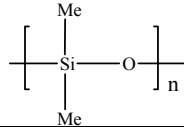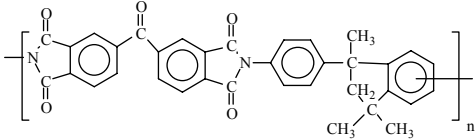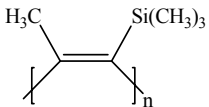
selectivity increased from 8 to 12.[26]   The O_2 permeability increase was attributed to dewetting around the Ag particle when pyrolyzing the membrane, which opened regions of voids. O_2/N_2 selectivity enhancement was attributed to the favorable adsorption of O_2 onto the Ag surface where surface diffusion may occur.

2.3 Reverse Selective Polymers for CO_2/H_2 Separations

As already discussed, the ideal polymer for separating CO_2 from H_2 should have solubility selectivity favoring CO_2. Additionally, the polymer should have a weak size-sieving ability to minimize the diffusivity selectivity. With some membranes, solubility selectivity is sufficiently high to offset unfavorable diffusivity selectivity, which makes the permeability selectivity favor the larger, more soluble penetrant.

Polymer membranes can be conveniently divided into four types of materials depending upon their reverse selective properties (*cf.* Table 1). Polymers can be either non-polar or polar, and they can be either glassy or rubbery. Polar polymers can have favorable interactions with polar gases.[11] For example, in copolymers of 71 % butadiene and 29% polar acrylonitrile, CO_2/N_2 selectivity is 29 at 25 $^{\circ}$C.[27] In non-polar polymers, solubility selectivity is generally lower. For example, rubbery poly(dimthylsiloxane) [PDMS] has a CO_2/N_2 solubility selectivity of 14.3 and a CO_2/N_2 permeability selectivity of 10 at 35 $^{\circ}$C.[28] CO_2/H_2 reverse selective behavior can become more favorable in some rubbery, polar polymers. For example, in crosslinked polyethylene oxide [XLPEO], CO_2/H_2 selectivity is 8 at 35 $^{\circ}$C,[29] and CO_2/N_2 permeability selectivity and solubility selectivity are 68 and 38, respectively, at 25 $^{\circ}$C and 3.4 atm.[30] Both PDMS and XLPEO are rubbery polymers, and their diffusivity selectivity is sufficiently weak that they are more permeable to CO_2 than to H_2 which is smaller.

Table 1. Polymer types, structure, and CO_2/H_2 selectivity

Polymer	CO_2/H_2 Selectivity at 35 °C, 3.4 atm	Fractional Free Volume	Properties	Structure
XLPEO[11]	6.4	0.12	Polar, Rubbery	
PDMS[33]	4	0.18	Non-polar, Rubbery	
PI[26,37]	0.3 (CO_2/He)	0.23	Polar, Glassy	
PTMSP[38]	1.6	0.29	Non-polar Glassy	

The selectivity of conventional, low free volume, glassy polymers is generally dominated by diffusivity selectivity. Low free volume glassy, polar polymers can have very strong size sieving capabilities, and smaller molecules (*e.g.*, H_2, He) are more permeable than larger molecules (*e.g.*, CO_2). For example, Matrimid 5218, a polyimide [PI], is 3.5 times more permeable to helium than to CO_2,[21] even though CO_2 is far more condensable (the T_c of He is 5.2 K, and it is 304 K for CO_2).[8] On the other hand, glassy PTMSP has a very high free volume, 0.29,[31] and it exhibits a CO_2/H_2 selectivity of 1.6.[9] The fact that PTMSP is more permeable to CO_2 than to H_2 is attributed to the poor size-sieving ability generally observed in high free volume, glassy polymers.[32]

It may be possible to use nanoparticles to enhance gas transport properties of membranes from each group of materials in Table 1. The non-polar materials have low CO_2/H_2 solubility selectivity. However, nanoparticles exist which adsorb large amounts of CO_2.[33] By adding such particles to non-polar polymers, nanocomposite solubility

selectivity may increase. Given a nanoparticle with sufficiently high CO_2 adsorption, the same approach might be applied to polar polymers. Glassy polymers tend to have strong size sieving capabilities due to low fractional free volume and highly restricted polymer segment mobility. The addition of nanoparticles to high free volume, glassy polymers can increase penetrant diffusion coefficients.[19] Additionally, nanoparticles reduce diffusivity selectivity (*e.g.*, C_2H_6 / *n*-C_4H_{10} diffusivity selectivity decreases from 5 to 1.5 when 50 wt. % FS is added to PMP at 25 °C).[19] Therefore, CO_2 sorbing nanoparticles may shift both CO_2/H_2 solubility selectivity and diffusivity selectivity in favor of CO_2/H_2 reverse selectivity for glassy polymers (*cf.* arrow A Figure 5). For rubbery polymers, where diffusion coefficients are expected to decrease with increasing nanoparticle loading, CO_2/H_2 selectivity may increase while the CO_2 permeability decreases (arrow B in Figure 5). Therefore, CO_2 adsorbing nanoparticles may provide a method for increasing CO_2/H_2 selectivity in both rubbery and glassy polymers.
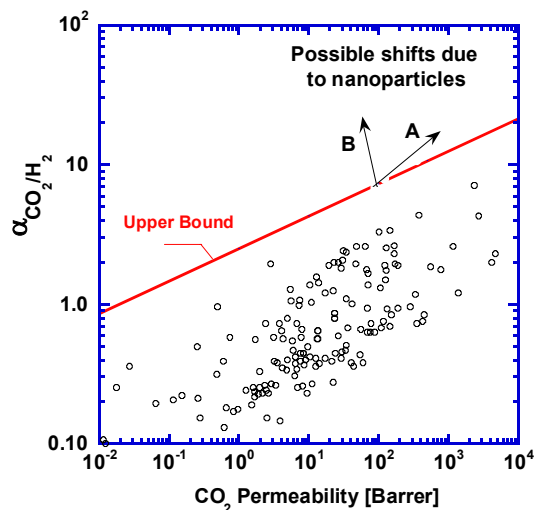
Figure 5. CO_2/H_2 permeability/selectivity map with upper bound and anticipated changes of CO_2/H_2 selectivity and CO_2 permeability due to incorporation of CO_2 adsorbing nanoparticles into polymers.

2.4 Gas Adsorbing Metals and Metal Oxides

Many metals and metal oxides adsorb certain permanent gases more favorably than others.[34-36] For instance, both clean iron and silver readily adsorb atmospheric oxygen without adsorbing other light gases.[34,35] Gases adsorb onto metals and metal

oxides by a variety of mechanisms depending on system chemistry (*e.g.,* acid-base interactions, gas dissociation, etc.),[13,33,37-39] overall system conditions (*e.g.,* temperature, pressure),[33,39] and surface defects[40] of the metal or metal oxides.

Since CO_2 is an acid gas, basic particles readily adsorb CO_2. For example, MgO adsorbs 10 wt. % CO_2 at ambient temperature and 20 Torr CO_2 after 15 minutes,[14] and CaO adsorbs 3.5 wt. % CO_2 at ambient temperature and 10 Torr CO_2.[41] In basic metal oxides, the oxygen atom withdraws electrons from the metal, causing the oxygen to behave as an electron-rich Lewis base and the metal to act as a Lewis acid.[42] The oxygen atoms of metal oxides interact with CO_2.[43] Basic metal oxides can adsorb CO_2 preferentially *vs.* light gases.[37,44]

There are substantial differences in the interactions of metal oxides with CO_2. At ambient temperatures, MgO physisorbs[42] or weakly chemisorbs CO_2,[45] whereas the heavier alkaline earth oxides tend to chemisorb CO_2.[37,38] The binding energy of CO_2 to metal oxides is due to the basicity of the alkaline earth oxides,[33] which increases with the period of the metal (*i.e.,* MgO is less basic than CaO, SrO is less basic than BaO, *etc.*).[37,38] Many rare earth metal oxides (*e.g.,* La_2O_3 and ThO_2) act as bases.[33] Rare earth oxides have a stronger binding energy and adsorb higher concentrations of CO_2 than alkaline earth oxides.[13,33] An ideal CO_2 adsorbing nanoparticle candidate would have a high CO_2 uptake while still being able to desorb CO_2.

Many inorganic materials catalyze reactions (*e.g.,* decomposition of CO_2 to CO on Fe_2O_3),[35] and such reactions could have deleterious effects if they were operative in separation membranes. In many systems, CO_2 and H_2 form CH_4, methanol or alkanes depending on the catalyst (*e.g.,* Ni, Ru, Cu).[46,47] The alkaline earth oxides react with water, which, in a subsequent reaction, can form metal carbonates.[48,49] Since CO is toxic and a poison for fuel cells, metals allowing decomposition of CO_2 to CO should not be used. Hydrogenation of CO_2 reverses the steam reforming reaction, which would reduce the overall efficiency of H_2 synthesis. Although water will be present in the H_2 product stream after steam reforming, carbonation is an acceptable side reaction since it does not produce harmful byproducts nor reduce system H_2 production efficiency. Possible reactions involving basic nanoparticles should not influence the chemical composition of gases permeating through the membrane.

MgO fits the criteria outlined above for CO_2 adsorbing materials, and it has other desirable attributes as well. CO_2 should readily desorb from MgO at 35 ^{0}C.[50] MgO nanoparticles are commercially available in particle diameters (3, 7, 12, 36 and 100 nm) in the size range of interest. Since gas adsorption cannot occur on defect-free, crystalline MgO surfaces,[51] ideal nanoparticles should offer a combination of high surface area and a large number of defect sites per unit area. Aerogel MgO has surface defects (*e.g.,* steps in the crystal, oxygen vacancies, *etc.*)[43] which permit gas adsorption,[43] and MgO particles are commercially available with surface areas greater than 600 m^2/g, which corresponds to an equivalent spherical particle diameter[b] of less than 3 nm. These particles are spherical, which results in a large percentage of surface sites being defects.[41] Therefore, MgO nanoparticles have been the focus of the nanocomposite portion of this study.

Other commercially available nanoparticle candidates are listed in Table 2. These materials are categorized by their reported surface chemistry. The basic nanoparticles are discussed above. Neutral and acidic particles may be used to contribute to a systematic study of the influence of particle-gas acid/base interactions on penetrant solubility and overall gas transport properties. Inert particles are those that are not expected to significantly adsorb nor interact (*i.e.*, acid/base, reaction, *etc.*) with CO_2.[52,53] Such materials may be used to provide examples of particles without specific surface chemistry interaction with CO_2.

Table 2: Nanoparticle Surface Chemistry and Commercially Available Particle Size

	Chemistry	Apparent Particle Diameter (nm)
SiO_2	Acidic[33]	10,15,80
TiO_2	Neutral[33]	5,10,15,40
MgO	Basic[33]	3,7,12,36
CaO	Basic[33]	8,25
BaO	Basic[38]	< 50
Ag	Inert[52]	30, 50

---

[b] Equivalent Spherical Particle Diameter = 6/(surface area x particle density)

3. Results

3.1 Experimental Technique

Nanocomposite Film Preparation: PTMSP was added to toluene at 1.5 g / 100 mL of solution and allowed to stir until the polymer was dissolved. Nanoparticles were added to the polymer solution and mixed using a Waring Handheld High Speed Blender at 15000 rpm for 15 minutes. Nanoactive^{TM} MgO Plus (Nanoscale, Manhattan, KS) particles were used throughout this study. They have a specific gravity of 3.58 g/cm^3 and a BET surface area between 600 - 700 m^2/g depending on the production lot.[54,55] The resulting equivalent spherical particle diameter was between 2.1 and 2.6 nm. Samples were spherical and 99.2% pure Mg based on metal.[55] MgO aerogels deagglomerate in many organic solvents, including toluene.[41] The nanoparticle/polymer solution was allowed to stir overnight with a magnetic stirring bar. The solution was then poured onto a clean, dry, level casting plate and allowed to cast until the toluene completely evaporated, which usually required two days. Due to the reactivity of MgO with water,[36] all sample preparation involving particles were conducted in a closed glove box under a N$_2$ blanket with a feed pressure between 1.5 and 5 cmH$_2$O gauge and a relative humidity of 0.0 as determined by a Testo 635 (Hotek Technologies) humidity indicator.

Permeability: Pure gas permeation measurements were conducted using a constant pressure/variable volume apparatus.[56] Films were not masked. Once a film was placed in the permeation cell, the film was exposed to the gas of interest for at least thirty minutes at test pressure to ensure that steady state permeation was established. Gas permeability (cm^3(STP) cm/(cm^2 s cmHg)) was calculated from the steady state rate of permeate flowrate in a downstream bubble flow meter according to:

$$P_A = \frac{273 p_{atm}}{T\,76} \frac{l}{A(p_2 - p_1)} \frac{dV}{dt} \tag{7}$$

where dV/dt is the permeate volumetric flowrate (cm^3/s), l is the film thickness (cm), p_2 is the upstream gauge pressure (cmHg), p_1 is the downstream gauge pressure (cmHg), p_{atm} is atmospheric absolute pressure (cmHg), A is the area of the film available for transport (cm^2), and T is absolute temperature (K). All experiments were performed with the downstream pressure at atmospheric (76 cmHg).

Pure- and mixed-gas permeation properties of membrane films evaluated at RTI were determined in a continuous-flow, constant-pressure/variable-volume apparatus modified with downstream sweep gas capability. A schematic of the RTI permeation system is shown in Figure 6. The entire permeation apparatus is contained in a thermoregulated enclosure (e.g., oven) for temperature control. The permeation cell holds the flat (planar) membrane film to be evaluated and has an effective permeation area of 13.8 cm^2. Mass flow controllers regulate the flow of feed and sweep gases to the permeation cell, and a metering valve controls the upstream (feed) pressure to the desired value. The permeation system is supported by two gas chromatographs (GCs), a Hewlett-Packard 5890 Series II GC with two thermal conductivity detectors (TCDs) for measuring the concentrations of non-sulfur gases and a Varian 3600 GC with one TCD and one flame photometric detector (FPD) for determining the concentrations of sulfur-containing gases. The GCs are interfaced to Agilent ChemStation data acquisition software to allow on-line analysis of feed, residue, and permeate stream compositions. Calibration of GC detector responses is performed by analyzing certified standards containing the gas components of interest.

Pressure gauge

Feed

Pressure regulator

MFC

Metering valve

Residue

Temperature control

Membrane cell

Permeate

Sweep

MFC

GC

To vent
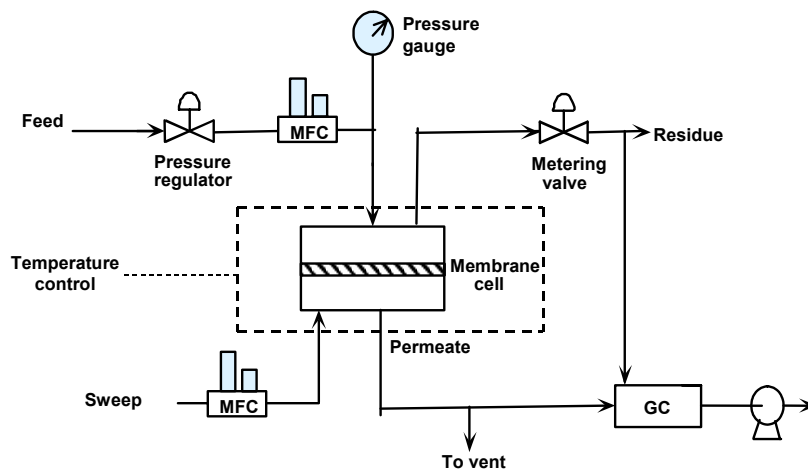
Figure 6. Schematic of gas permeation apparatus at RTI.

Permeation properties of membrane films were first characterized with pure gases, such as N_2, O_2, H_2 and CO_2, to check integrity. Separation performance of defect-free membranes were then evaluated with either a binary gas mixture (e.g., 25%

CO_2 in H_2) or a simulated, four-component, coal-derived synthesis gas consisting of 1% H_2S, 36% H_2, and 13% CO_2 in CO. In all tests, the upstream (feed) pressure was typically 50 or 100 psig, and the downstream (permeate) pressure was kept at atmospheric (0 psig). To control the emission of sulfur gases, the permeate and residue streams were passed through ZnO sorbent beds to scrub out any H_2S present before venting to the atmosphere.

Solubility: An automated spring balance for kinetic gravimetric sorption has been used to determine the solubility of pure permanent gases and CO_2 in nanocomposite samples.[57] An analytical balance was used to determine film weight. The film was placed on a quartz spring (Ruska Instruments, Houston, TX) so that the spring reference pointer was below a reference rod. An initial reading of spring extension was recorded. Vacuum was applied overnight to degas the film and the system. At this point, a second reading of spring extension was taken to determine the weight loss due to degassing:

$$W_f = W_l - k(l_i - l_v) \tag{8}$$

where W_l is the loaded weight of the film (mg), k is the spring constant (mg/mm), l_i is the initial spring extension, and l_v is spring extension after the sample has been evacuated for at least 24 hours.

Spring extension data were acquired while the sample was exposed to CO_2 at a set pressure for 20 minutes. After twenty minutes, the system pressure was increased and testing was repeated until system pressure was just below atmospheric pressure (the limit of testing for this apparatus). Gas concentration in the film was calculated as follows:

$$C = \frac{22414 \rho k (l_p - l_v)}{W_f M_w} \tag{9}$$

where ρ is the film density (g/cm^3), l_p is the spring extension after 20 minutes at a given pressure (mm), and M_w is the molecular weight of the test gas.

Density measurements: Density was measured via a hydrostatic weighing method. A Mettler Toledo balance (Model AG204, Switzerland) and a density determination kit were used. Samples were tested in deionized water.

Atomic Force Microscopy (AFM): Tapping mode AFM (Digital Instruments Dimension 3100 with Nanoscope IV controller, Woodbury, New York) was used to characterize particle dispersion at the nanocomposite surface. The AFM tips are Silicon NCH (Nanosensors, now Nanoworld, Neuchatel, Switzerland). The height, amplitude, and phase profile were examined. Samples were tested at 1 μm x 1 μm with 512 lines scanned per sample, providing a resolution of 2 nm, (resolution = length of sample side/number of scans per sample). The scan rate was 0.2 Hz or 0.8 μm/s. Integral and proportional feedback settings were 0.4 and 0.75, respectively.

Fourier transform infrared spectroscopy (FTIR): FTIR (Thermo Nicholet Nexus 470, Madison, WI) was used to examine particle-polymer interactions or reactions. The crystal was cleaned with isopropyl alcohol (Aldrich) prior to acquiring a background signal. The background signal was always recorded prior to testing samples. Samples were measured immediately after removal from the glove box whenever possible.

X-ray photoelectron spectroscopy (XPS): XPS (PHI 5700, Physical Electronics Company) was used to examine films for evidence of chemical reactions. Films were submitted to Dr. Yangming Sun of the Texas Materials Institute for examination.

Hydrogen, Carbon & Silicon Nuclear Magnetic Resonance (^{1}H NMR), (^{13}C NMR) & (^{29}Si NMR): ^{1}H, ^{13}C, and ^{29}Si NMR spectra were acquired using a Unity +300 (Varian, Palo Alto, CA) NMR maintained and operated by the Analytical Services Laboratory of the Department of Chemistry and Biology. NMR sample materials were 1 to 2 wt. percent solids dissolved in solution.

Wide Angle X-ray Diffraction (WAXD): Wide angle X-ray diffraction (WAXD) was used to characterize the dispersion of nanoparticles in the polymer matrix. A Bruker-Nonius D8 Advance Theta-2Theta Powder Diffractometer, with CuKα radiation of 1.54 Å wavelength, was used for the experiments.

3.2 Definition of Volume Fraction

Generally, nanoparticle loading is reported in terms of weight %. However, this approach fails to give meaningful comparisons when nanoparticles of differing densities are used, or when particle or polymer density changes after the films have been made. Furthermore, characteristics of the nanocomposites such as density and estimates of

interparticle spacing and fractional free volume are dependant on the volume fraction of the filler. Therefore, it is necessary to provide a meaningful estimate of filler volume fraction before discussing the influence of MgO nanoparticles on gas transport properties of polymers.

There are two methods of discussing particle volume fraction in this report. First, a nominal filler volume fraction, ϕ_F^N, is defined. This volume fraction is based on the additive model value for volume, and it neglects the creation of void space (*i.e.,* the decrease in polymer density) with increasing filler loading. This volume fraction is calculated as follows:

$$\phi_F^N = \frac{W_F / \rho_F}{\left(W_P / \rho_P + W_F / \rho_F\right)} \tag{10}$$

where W_F and W_P are the weight percents of filler and polymer in the sample, and ρ_F and ρ_P are the densities of pure filler and pure polymer, respectively. Using ϕ_F^N is most informative when reporting information with controlled incremental changes in filler loading. The second method is referred to as the true filler volume fraction, ϕ_F^T, which is calculated from the experimental density of the nanocomposite while taking into account the potential existence of void fraction in the nanocomposite. The true filler volume fraction is calculated as follows:

$$\phi_F^T = \frac{\phi_F^N\left(\dfrac{W_P}{\rho_P} + \dfrac{W_F}{\rho_F}\right)}{\left(\dfrac{W_P}{\rho_P} + \dfrac{W_F}{\rho_F} + V_V\right)} = \frac{\left(\dfrac{W_F}{\rho_F}\right)}{\left(\dfrac{1}{\rho_C}\right)} = W_F \frac{\rho_C}{\rho_F} \tag{11}$$

where ρ_C is the composite density, and V_V is the void volume. This method of reporting filler volume fraction may be best suited for discussing experimental results and comparing to theoretical models. Figure 7 shows the large difference between ϕ_F^N and ϕ_F^T particularly at high particle loadings. However, ϕ_F^T will be used when discussing filler volume fraction-sensitive data (*e.g.,* interparticle spacing, relative solubility, *etc.*).
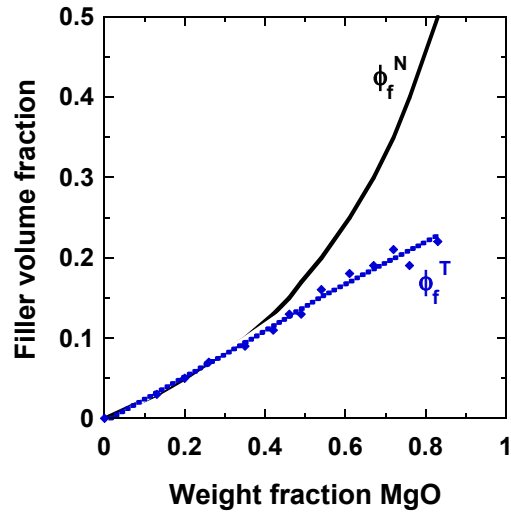
Figure 7. Estimated filler volume fraction using ϕ_F^N (—) and ϕ_F^T (♦) with increasing wt. fraction of MgO in PTMSP.

3.3 PTMSP-MgO Interactions

Two fundamental questions regarding nanocomposites are: (1) are the particles well-dispersed in the polymer matrix, and (2) how extensively does the polymer matrix wet the particles? Since these two questions are inherently interdependent, similar arguments are used to describe degree of mixing and particle wetting.

Interaction between the acidic TMS groups on PTMSP and basic metal oxides facilitates wetting between particles and polymer segments. According to the Pauling scale,[58] the electronegativity difference between carbon and silicon is +0.7 units, which indicates that the silicon electrons will be attracted towards the carbon atoms. Trimethylsilylbenzene [TMSB], shown in Figure 8, illustrates the TMS electronic properties when it is bound to an organic, conjugated molecule. TMSB has a dipole moment of 0.45 Debye,[59] and the TMS silicon is electron poor based on studies with halogenated derivatives of TMSB.[60] Therefore, the TMS Si has a slight positive charge. The silicon atom of the TMS group is electron donating and behaves like a Lewis acid, and the TMS carbon atoms act as Lewis bases. In MgO, magnesium atoms are very electron poor and act as Lewis acids, whereas oxygen atoms are electron rich and act as Lewis bases.[42] There is an acid/base interaction between the PTMSP silicon atoms and MgO oxygen atoms, and between the Lewis base carbon atoms of the TMS groups with

the Lewis acid Mg atoms of MgO. These acid/base interactions are believed to facilitate good wetting of the particles by the polymer segments.

$$\text{—} \underset{|}{\overset{|}{Si}} \quad \delta^+ \qquad \qquad \delta^-$$
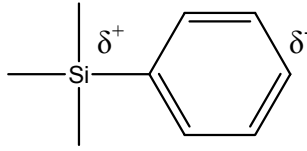
Figure 8. Structure of Trimethylsilylbenzene

AFM has been used to characterize the mixing of inorganic and organic particles in polymer matrices.[61-63] Khanna *et al*. used AFM to characterize the dispersion of glass fibers in polyester.[63] AFM has also been used to characterize the dispersion of a soft rubbery polymer (styrene-ethylene-butadiene-styrene with grafted maleic anhydride) in a hard polymer (nylon 6).[64] Dispersion was characterized by comparing particle size and shape using the AFM tapping phase profile.[64] This project uses the same technique to investigate particle dispersion in polymer matrices.

Figures 9 a-f show surface tapping mode AFM height and phase profiles for nanocomposites where ϕ_F^N is 0.13, 0.20, and 0.25 volume fraction MgO. In height profiles, black and white represents elevations of 0 and 250 nm, respectively. From Figures 8 a, c, and e, the height profile has few topographical features, which is consistent with good mixing since large agglomerates are not obviously present. In poor mixing, large agglomerates of particles would be expected to be present and readily observed. Such agglomerates are noticeably absent in the PTMSP – MgO nanocomposites.

In the phase profiles, black and white represent the softest and hardest phases, respectively, in the material under study. In this case, the soft phase is PTMSP, and the hard phase is MgO. The white phase is at least 25° out of phase, where "out of phase" denotes a detected phase lag between the cantilever signal and the driving signal sent to the piezo actuator.[65] Phase profiles are shown in Figures 9 b, d, and f. In all three nanocomposites, the particle phases are 3 – 8 nanometers in characteristic dimension as determined using the Particle Analysis option of the Nanoscope software. This result suggests that the particles are not agglomerating to a large extent.
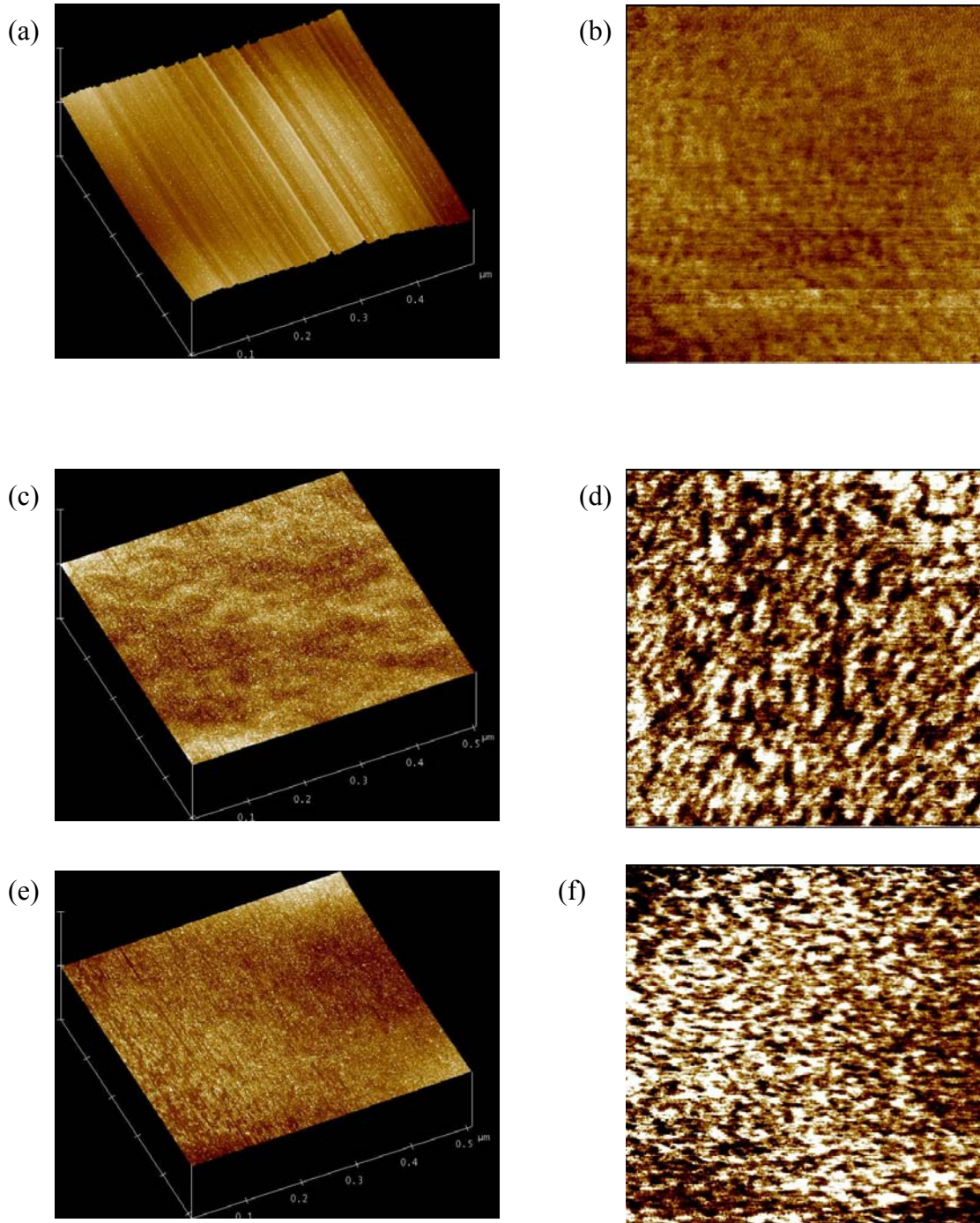
Figures 9. Tapping mode AFM images of the surface of an MgO filled PTMSP film. Images are 500 nm x 500 nm. (a,c,e): Height profiles of ϕ_F^N = 0.13, 0.20, and 0.25 volume fraction MgO, respectively, with white being 250 nm. (b,d,f): Phase profiles of ϕ_F^N = 0.13, 0.20, and 0.25 volume fraction MgO, respectively, where white is 25° out of phase. White indicates a hard phase. Black indicates a soft phase.
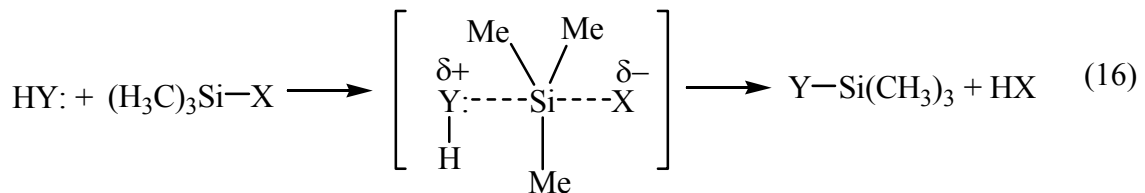
3.4 Evidence for a Desilylation Reaction

To date, the addition of nanoparticles to polymer membranes has involved no discernable change in the chemical structure of either the nanoparticle or the polymer.[10,26,66] Furthermore, there is no mention of desilylation of PTMSP in the open literature. However, the possible existence of polymer-particle acid/base interactions led to the exploration of chemical changes in MgO filled PTMSP films. A reaction was discovered between PTMSP and MgO. The first step in the reaction mechanism appears to involve the reaction between MgO and water to form $Mg(OH)_2$.[36] Although the nanocomposite solution and films are prepared in a glove box where we try to maintain an anhydrous environment, there may be some traces of water dissolved in the solvent, adsorbed on glassware and/or the polymer. The reaction of MgO with water is as follows: [36]

$$MgO + H_2O \longrightarrow Mg(OH)_2 \tag{14}$$

Next, PTMSP reacts with the $Mg(OH)_2$ alcohol groups. The proposed reaction is:

$$Mg(OH)_2 + \underset{(H_3C)_3Si}{\overset{CH_3}{C=C}} \longrightarrow HOMgOSi(CH_3)_3 + \underset{H}{\overset{CH_3}{C=C}} \tag{15}$$

The –OH group of $Mg(OH)_2$ is electron rich and very basic (pH 9.5 -10.5).[54] The basic alcohol lone pair electrons form a p-d bond with the trimethylsilyl group silicon.[67] Desilylation is most probable when the TMS donor is less basic than the acceptor, and the donor is conjugated to stabilize the p-d bond.[67] In PTMSP, the polymer backbone serves as the TMS donor, and it is less basic than MgO. Also, the polymer backbone is somewhat conjugated,[32] which allows for p-d bond stabilization. Eq. 15 shows an example of the typical pathway for a desilylation reaction: [67]

$$HY: + (H_3C)_3Si-X \longrightarrow \left[\underset{H}{\overset{Me \quad Me}{\underset{\delta+}{Y}\cdots\underset{|}{Si}\cdots\overset{\delta-}{X}}} \right] \longrightarrow Y-Si(CH_3)_3 + HX \tag{16}$$

where Y is the TMS acceptor (HOMgO$^-$ in this case) and X is the TMS donor (the PTMSP backbone). The lone pair electrons on Mg(OH)$_2$ form a p-d bond with silicon. The p-d bond is stabilized by conjugation with the PTMSP backbone. The final step requires that the alcohol hydrogen transfer to the polymer backbone while the Si-C bond is broken.[67]

FTIR spectra of PTMSP and a nanocomposite are shown in Figure 10. MgO does not absorb in the range shown. Differences between the two spectra are expected at 3740 cm^{-1} for Mg-OH[68] and in the range of 1400 – 1650 cm^{-1} for carbonate formation.[69,70] A broad peak exists in the nanocomposite spectrum at 1092 cm^{-1}, which is not predicted in the literature for either pure MgO, Mg(OH)$_2$, or PTMSP. This peak is consistent with the presence of X-O-Si bonds,[71] and it is attributed to the formation of Mg-O-Si.
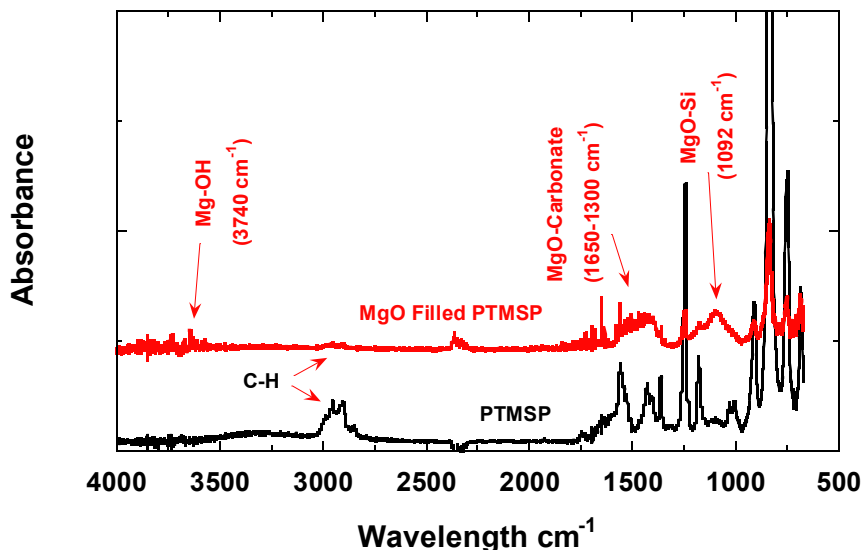
Figure 10. FTIR spectra of PTMSP and PTMSP filled with MgO $\left(\phi_F^N = 0.20\right)$.

Silicon 2p orbital XPS on a PTMSP/MgO nanocomposite shows Si has bonds to two different elements (*cf.* Figure 11). The peak at 101 eV corresponds to Si-C bonds,[72] while the peak at 105 eV represents Si-O.[73] The only oxygen source in filled PTMSP is MgO and/or Mg(OH)$_2$. Therefore, XPS corroborates the existence of the Mg-O-Si bond.
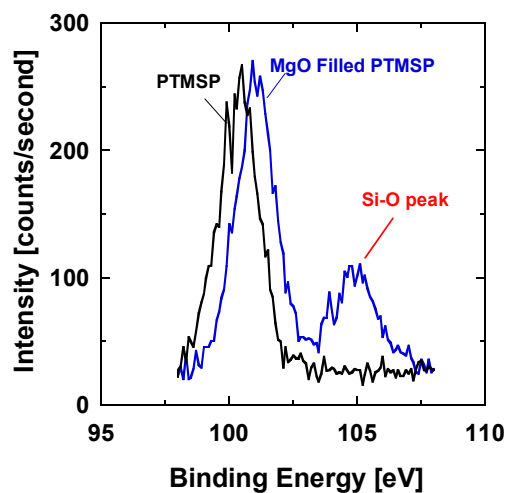
Figure 11. XPS of Si 2p orbital for PTMSP and MgO filled PTMSP $\left(\phi_F^N = 0.20\right)$.

Solution ^{1}H NMR spectroscopy was conducted on polymer nanocomposites to determine if changes had occurred in the polymer structure due to the reaction.   A singlet peak exists at 3.8 ppm for MgO filled PTMSP, which indicates an olefinic proton (compare Figures 12(a) and 11(b)). Since PTMSP does not have a peak at 4.3 ppm, the olefinic peak proton must be a product of the desilylation reaction. The ^{1}H NMR integral data indicates that 9 % of the TMS groups have been removed from the polymer. The presence of the olefinic proton provides additional evidence for the existence of the MgO-PTMSP desilylation reaction.
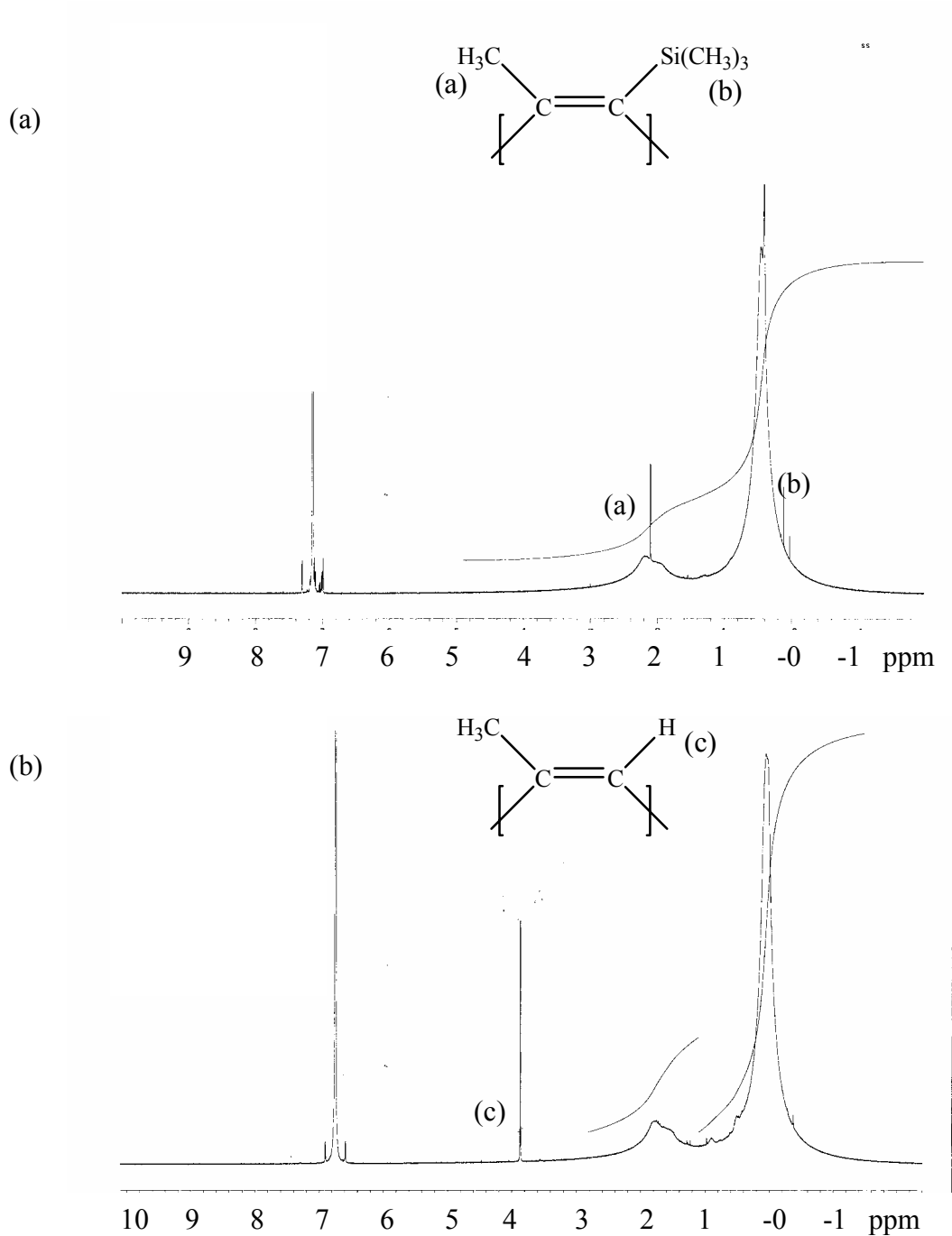
Figure 12. ^{1}H NMR of (a) PTMSP and (b) MgO filled PTMSP $\left(\phi_F^N = 0.20\right)$.

A small molecule analog of PTMSP was selected to study desilylation in the presence of MgO. The molecule studied was 1-phenyl-2-(trimethylsilyl)acetylene [PhTMSA], whose chemical structure is shown in Figure 13. The aromatic group of

PhTMSA mimics, to a certain extent, conjugation of the PTMSP backbone and stabilizes oxygen-silicon p-d bonds. Thus, the TMS donor group should exhibit chemistry similar to that of PTMSP.
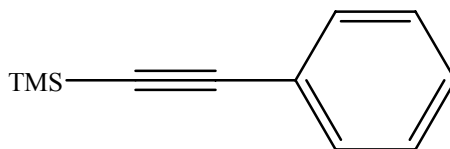
Figure 13. Chemical structure of 1-Phenyl-2-(trimethylsilyl)acetylene (PhTMSA).

Figure 14 shows the FTIR spectrum of PhTMSA treated with MgO after having the untreated PhTMSA spectrum subtracted. The MgOH bond peak is present at 3740 cm^{-1}, which indicates that the water-MgO reaction takes place. The MgO-Si peak is present at 1092 cm^{-1}, indicating that the desilylation reaction has occurred.
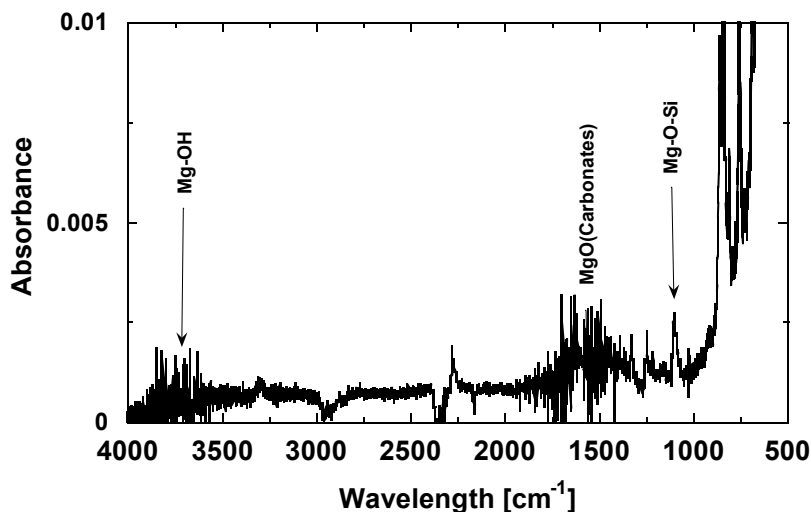
Figure 14. Subtraction of untreated PhTMSA FTIR spectrum from MgO treated PhTMSA FTIR spectrum.

There are three new peaks in the ^{1}H NMR spectrum of MgO treated-PhTMSA (compare Figures 15(a) and 15(b)). These peaks are at 7.39, 2.72, and 0.10 ppm. The peak at 7.39 ppm (g,h) corresponds to the *m*-phenyl protons on the desilylated PhTMSA samples. The peak at 2.72 ppm (e) corresponds to the proton bound to an acetylene unit, which confirms the hydrogen-TMS transfer between Mg(OH)$_2$ and PhTMSA. The peak

at 0.1 ppm (i) peak corresponds to the MgOTMS protons. The MgOTMS/acetylene proton integral ratio is 9:1, which is the stoichiometric ratio of the reaction (*cf.* Eq. 15). The PhTMSA TMS proton integral value is 6. The MgOTMS proton integral value of 9 is divided by the total proton integral value of 15 to estimate the extent of desilylation, which is 60%.
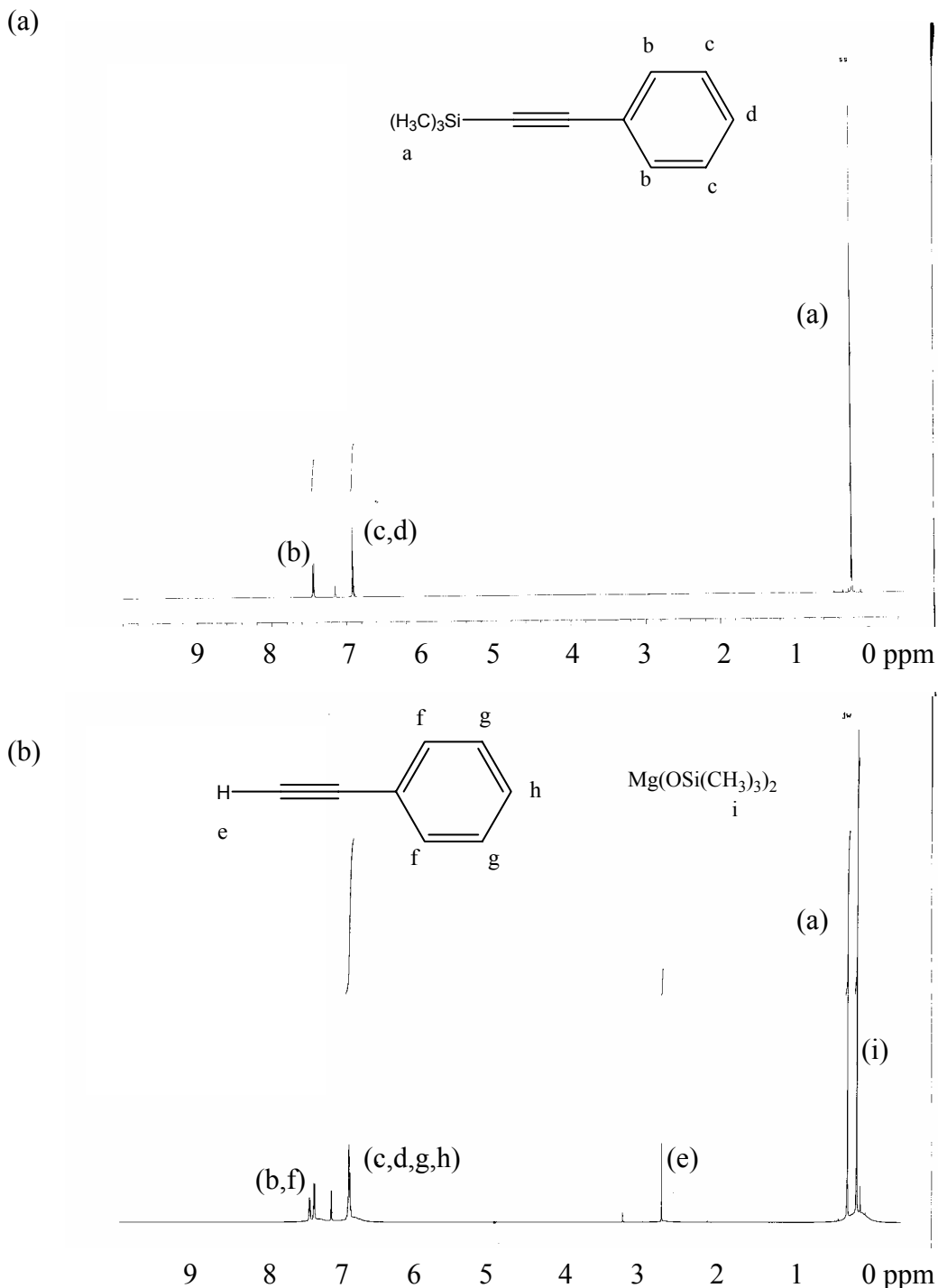
Figure 15 ^{1}H NMR of (a) PhTMSA and (b) PhTMSA treated with MgO.

The ^{13}C NMR spectrum shows a definite chemical change when PhTMSA is contacted with MgO (compare Figures 16(a) and (b)). The peaks at 106 ppm (c) and 94 ppm (b) represent the acetylene carbon, while the peak at 0 ppm (a) corresponds to the TMS carbons. However, three peaks appear at 84, 78 and 2 ppm. The peaks at 84 ppm (i) and 78 ppm (h) represent desilylated acetylene carbons. The peak at 2 ppm (n) is attributed to MgO(TMS), which is present due to its high concentration in the solution (60% as calculated from ^{1}H NMR).
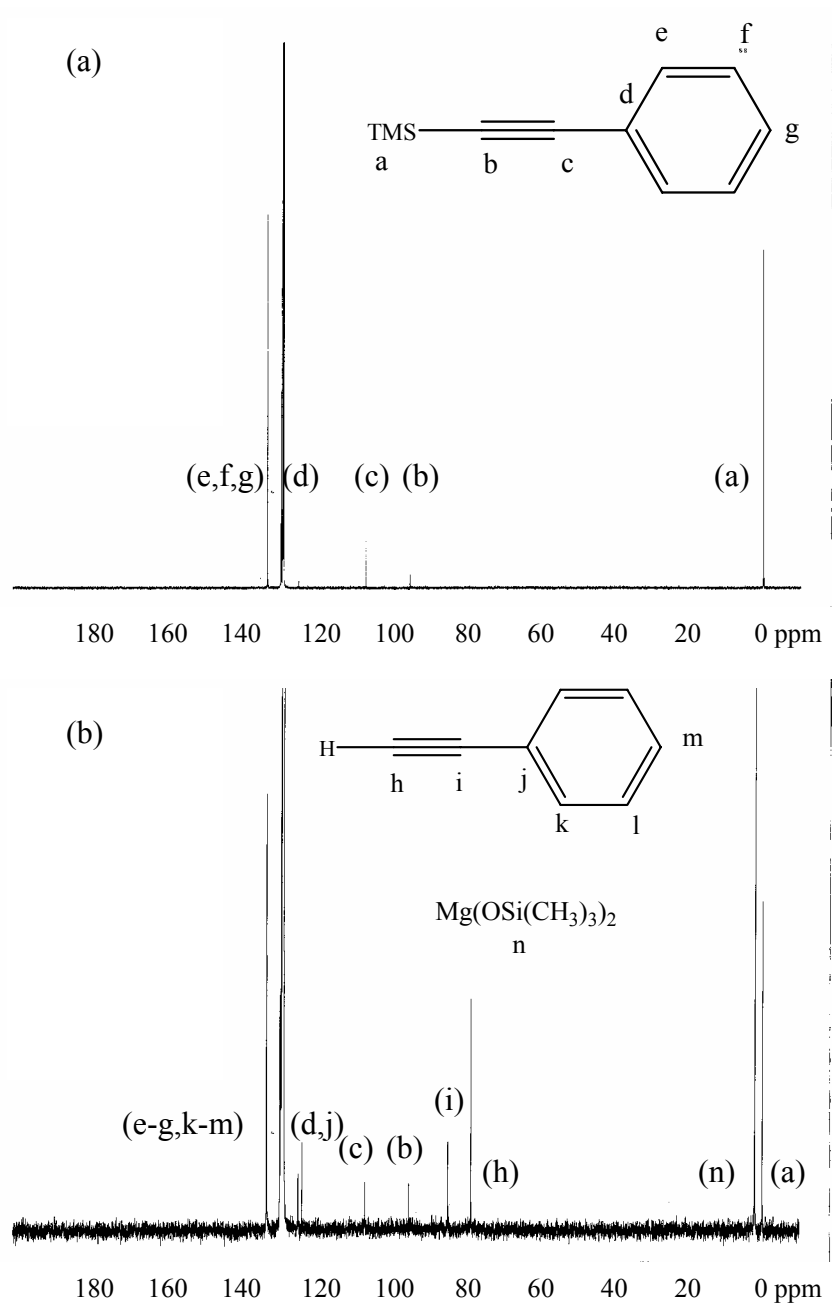
Figure 16 ^{13}C NMR of (a) PhTMSA and (b) PhTMSA treated with MgO.

Figures 17(a) and (b) show that the ^{29}Si NMR spectra of a mixture of MgO $\left(\phi_F^N = 0.13\right)$ and PhTMSA does not exhibit the strong peak at -20 ppm that is observed in neat PhTMSA. The loss of the peak indicates desilylation of PhTMSA. Although complete desilylation has not been observed in the ^{13}C and ^{1}H spectra, the extent of reaction is sufficient to lower the peak intensity of PhTMSA below the detection limit in this experiment. The peak at -105 is the silicon in the NMR tube.
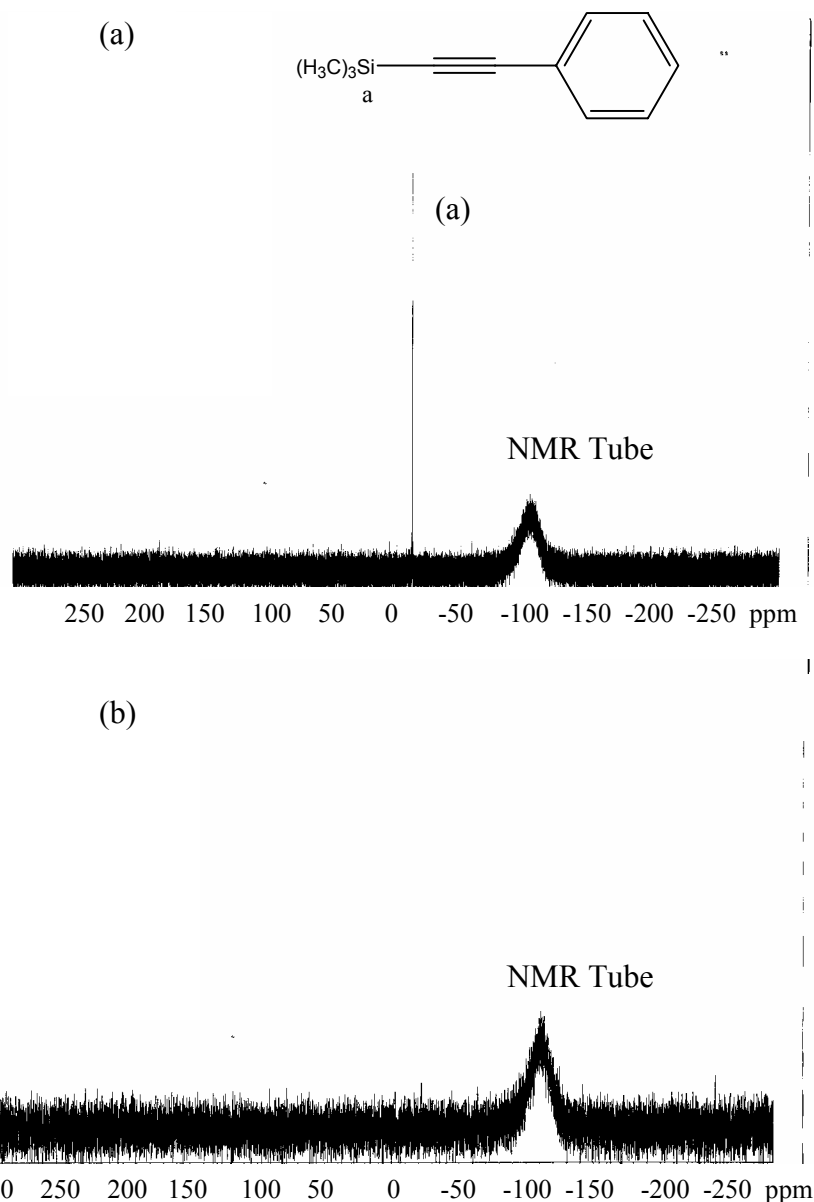
Figure 17 ^{29}Si NMR of (a) PhTMSA and (b) PhTMSA treated with MgO.

3.5 MgO-PTMSP Gas Transport Properties

This work was based on two hypotheses regarding gas transport: (1) MgO nanoparticles may enhance gas transport properties by increasing the void fraction of the nanocomposite, (2) MgO may enhance the solubility properties of nanocomposites. Figure 18 shows the permeability ratio of nanocomposite films with increasing MgO loading, where permeability ratio is defined as the permeability of the nanocomposite divided by the permeability of neat PTMSP. At a nominal volume fraction of 0.3 MgO, nanocomposite membranes exhibit a pure gas CO_2/H_2 selectivity of 1.6, which is equivalent to that of pure PTMSP.[9] For the same film, the CO_2 permeability is greater than 122,000 Barrer, which is the highest CO_2 permeability ever reported for a polymer membrane.
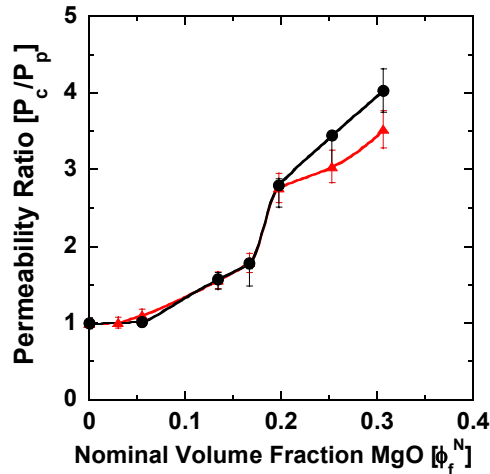
Figure 18. Gas permeability ratio, the permeability of the composite, P_C, divided by the permeability of the polymer, P_P, of mixtures of PTMSP with increasing nominal volume fraction MgO, ϕ_f^N, content at 35 ^{o}C and $\Delta p = 3.4$ atm. CO_2 (▲); H_2 and N_2 (●).

The experimental density of PTMSP-MgO nanocomposites is lower than the density based on a simple additive model (*cf.* Figure 19). The composite density based on the additive model, ρ_A, is calculated as follows:

$$\rho_A = \rho_F \phi_F^N + \rho_P \phi_P^N \tag{17}$$

where ρ_P and ρ_F are the polymer and filler density, and ϕ_P^N is calculated as follows:

$$\phi_P^N = \frac{W_P / \rho_P}{\left(W_P / \rho_P + W_F / \rho_F\right)} \tag{18}$$

where W_P and W_F are the weight fractions of polymer and filler in the composite, and ρ_P and ρ_F are the nominal densities of polymer and filler, respectively. The difference between the measured density of the composites and that estimated from the additive model is ascribed to an increase in the volume fraction of void space (or free volume) in the nanocomposite, which was calculated as follows:

$$\phi_V = 1 - \frac{\rho_C}{\rho_F \phi_F^N - \rho_P \phi_P^N} \tag{19}$$

where ϕ_F^N is the nominal filler volume fraction calculated by Eq. 11, and ϕ_P^N is the nominal polymer volume fraction calculated from Eq. 18. Figure 20 shows that the volume fraction of voids, ϕ_V, increases with increasing particle loading.
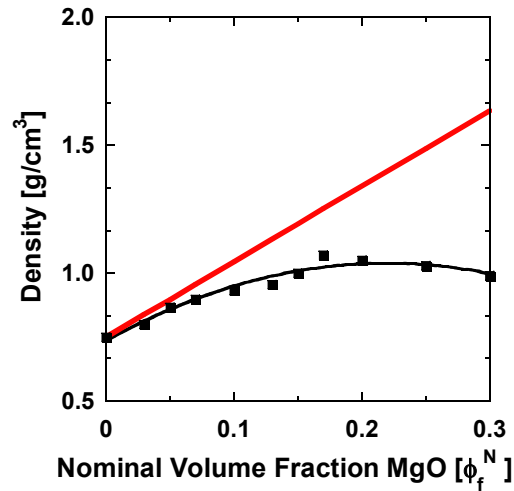
Figure 19. Density of PTMSP MgO composites as a function of nominal volume fraction , ϕ_F^N , in the mixture (■). The solid straight line is the prediction of the volume additivity model (Eq. 17).
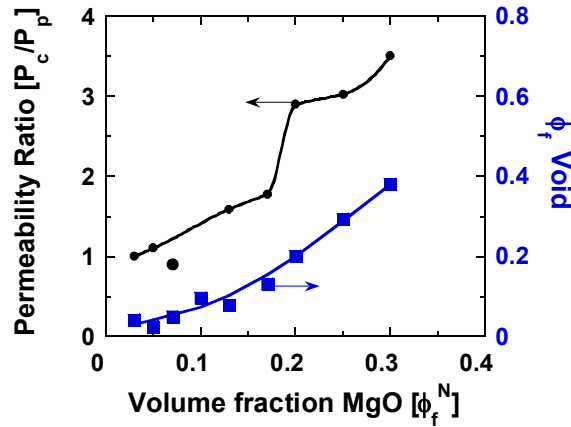
Figure 20. Nanocomposite void fraction (■) and CO_2 permeability ratio at 35 ^{o}C and Δp = 3.4 atm (●) as a function of nominal MgO volume fraction, ϕ_F^N.

Pure gas selectivity remains unchanged with increasing particle loading. The particles do not introduce interconnected defects that span the film. Such defects would reduce selectivity to values consistent with bulk flow through pores or Knudsen flow, depending on the size of the defect.[74] In Knudsen flow, CO_2/H_2 permeation selectivity would be 0.2, which is calculated as follows: [74]

$$\alpha_{A/B} = \sqrt{\frac{M_B}{M_A}} \tag{20}$$

where M_A and M_B are the molecular weights of gases A and B, respectively. In bulk flow, the CO_2/H_2 selectivity would be 1.

The particle diameter is near the dimensions of a monomer unit of PTMSP (calculated to be 0.65 nm) and similar to the length of a CO_2 molecule, 0.51 nm.[43] Interparticle spacing can be crudely estimated by assuming that the particles are ideally packed. For the calculations that follow, a cubic lattice structure is used because of its simplicity, and because it corresponds well with data presented later. The cubic lattice interparticle distance, d_i, is calculated as follows:

$$d_i = \left\{ \left(\frac{4\pi}{3} \left[\frac{d_F}{2} \right]^3 \right) \frac{1}{\phi_F^T} \right\}^{\frac{1}{3}} - d_F = \left(\frac{\pi d_F^3}{6\phi_F^T} \right)^{\frac{1}{3}} - d_F \qquad (21)$$

where d_F is the particle diameter, and ϕ_F^T is the true particle volume fraction. In this calculation the cubic lattice cell volume is estimated by dividing the volume of a single particle by the true filler volume fraction. The cube root is then taken of the lattice cell volume to estimate the cell dimensions, from which the particle diameter is substracted to obtain an estimate of interparticle distance.

Interparticle spacing may have a strong influence on void space and permeation properties of the nanocomposite films. At ϕ_F^T values above 0.05, and using a particle diameter of 2.5 nm, the ideal cubic interparticle spacing is on the order of 3 nanometers or less (*cf.* Figure 21). PTMSP has three structural conformations (cis-transoid [CT], trans-cisoid [TC], and trans-transoid [TT]), (*cf.* Table 4).[32] At ϕ_F^T values above 0.19, the width of a single CT or TC PTMSP monomer unit cannot be accommodated by the estimated interparticle spacing. The width was calculated using the covalent radii for hydrogen, carbon, and silicon for each structural conformation from the outer most hydrogen for the TMS group on a polymer segment to the furthest hydrogen on the next polymer segment. For TC and CT structural conformations, this distance is calculated from the furthest hydrogen on opposing TMS groups, whereas for TT conformations it is calculated from the hydrogen on the TMS group to the hydrogen of the methyl group on an adjacent monomer unit of PTMSP. The absence of polymer in the interparticle space may introduce a significant amount of void space, which may be accessible to gas molecules. Therefore, much of the void fraction increase observed in the nanocomposites may be due to interparticle voids. These voids are believed to be separated by PTMSP chains and particles. Due to the excellent polymer-particle wetting and the particles impermeability, penetrant molecules must permeate through the polymer during at least part of their voyage across the film. Thus, the polymer selectivity is maintained in the nanocomposite.
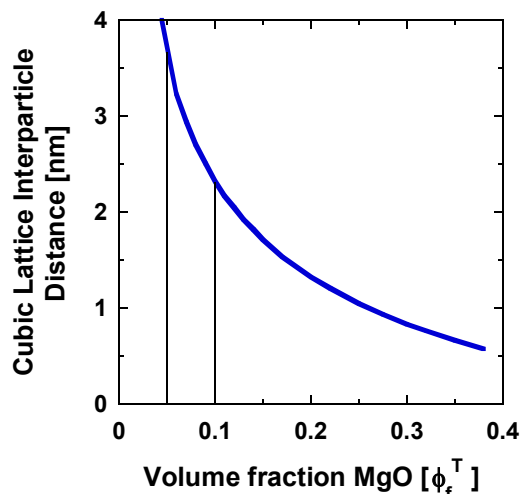
Figure 21. Calculated interparticle spacing assuming an ideal dispersion of monodisperse 2.5 nm diameter particles in a cubic lattice Eq. 21 was used for this calculation.

Table 4. PTMSP structure, width and MgO loading required to achieve an interparticle distance equal to PTMSP structural width.

PTMSP Structure	Width (nm)	Volume Fraction MgO (ϕ_F^T) when Width = interparticle distance
Cis-Transoid	1.1	0.19
Trans-Cisoid	1.1	0.19
Trans-Transoid	0.8	0.27

As shown in Figure 22, MgO adsorbs inert gases as well as CO_2. Figures 23 and 24 present CO_2 and N_2 relative solubility as a function of MgO volume fraction. These figures also include an estimate of the interparticle spacing, d_i, calculated from Eq. 21. At low loadings of MgO (*i.e.,* ϕ_F^T below 0.13), PTMSP may inhibit the efficient adsorption of penetrant molecules on MgO by covering the particle surface. However, as the MgO loading increases, there may be insufficient PTMSP to cover the MgO particles.

At these loadings (*i.e.,* ϕ_F^T greater than 13 volume percent MgO), MgO particle surfaces may be exposed to the penetrant gases, which allow for gas adsorption by the particles.
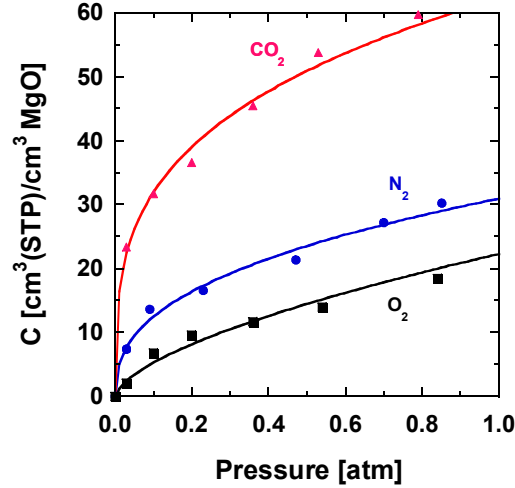
Figure 22. Concentration of CO_2 (▲), N_2 (●), and O_2 (■) on 2.5 nm diameter MgO particles at 35 °C.
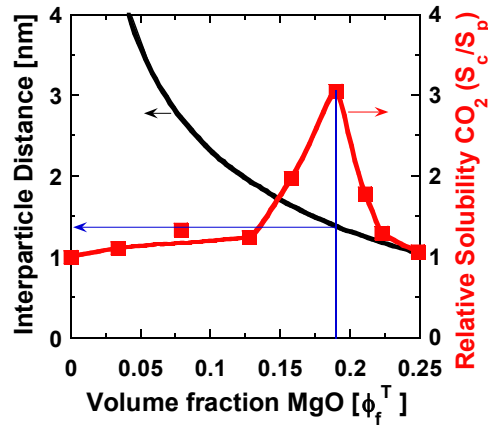
Figure 23. The effect of MgO content on relative CO_2 solubility and estimated interparticle distance in PTMSP/MgO nanocomposites. The MgO particles were 2.5 nm in diameter. Solubility is reported at 35 °C and 3.4 atm. Relative solubility is the ratio of the solubility of the nanocomposite to that of the neat PTMSP. The interparticle distance was estimated using Eq. 21.
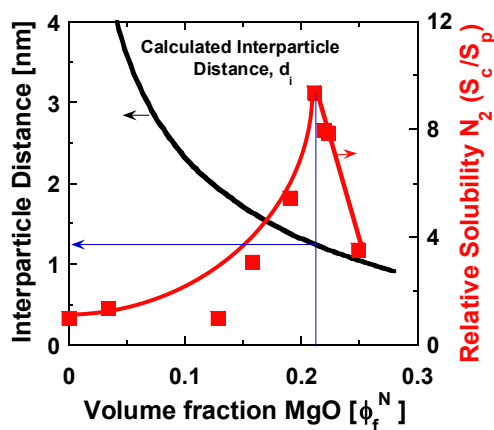
Figure 24. The effect of MgO content on relative N_2 solubility and estimated interparticle distance in PTMSP/MgO nanocomposites. The MgO particles were 2.5 nm in diameter. Solubility is reported at 35 °C and 3.4 atm. Relative solubility is the ratio of the solubility of the nanocomposite to that of the neat PTMSP. The interparticle distance was estimated using Eq. 21.

The relative solubility for both CO_2 and N_2 has a maximum. The CO_2 relative solubility maximum occurs at a true particle volume fraction near 0.17, where the interparticle distance is calculated to be 1.3 nm from Eq. 21. CO_2 is known to form carbonates on the surface of MgO, which correspond to a range of 1300-1650 cm^{-1} in FTIR.[68,69] Such carbonate peaks are observed for MgO filled PTMSP nanocomposites, (*cf.* Figure 10). The distance of the carbonate oxygen atoms from the MgO surface has been calculated to be 0.68 nm.[45] The interparticle spacing where the CO_2 relative solubility maximum occurs roughly corresponds to the interparticle distance required for carbonate formation on the opposing surface of two adjacent MgO particles. At higher MgO loadings, (*i.e.,* $\phi_F^T > 0.2$), the interparticle space is calculated to be less than 1.3 nm, which is not enough space for the formation of two carbonates between opposing particles. Therefore, the CO_2 relative solubility peak may occur due to insufficient interparticle space for carbonate formation on opposing particle surfaces at high MgO loadings.

The N_2 relative solubility maximum occurs at a true particle volume fraction of 0.21. The interparticle distance for this loading is 1.0 nm as calculated from Eq. 21.

Since, there is no analogous reaction of N_2 with MgO comparable to carbonate formation, the N_2 relative solubility peak cannot be justified using such an argument. There is currently no explanation for the relative solubility maxima which could apply to both CO_2 and N_2. However, these peaks may be related to a combination of gas-particle interactions and/or steric constraints placed on sorption due to interparticle distances.

3.6 Addition of 3-Methyl sulfolene Adsorbent to PTMSP and Pebax

Sulfolanes and sulfolenes are physical adsorbents that are used in formulations to remove acid gases such as CO_2 and H_2S from natural gas and reformate gas (Ref. http://www.cpchem.com/specialty_chemicals_a_cleaning_extraction.asp). 3-Methyl sulfolene ($C_5H_8SO_2$) was selected as a possible additive that might be compatible with useful polymer/solvent systems such as the PTMSP/toluene and Pebax/*n*-butanol systems. Hence, in an initial attempt to improve the acid-gas/H_2 selectivity of glassy PTMSP homopolymer and a rubbery Pebax block copolymer, 3-methyl sulfolene crystals were physically dispersed as filler at concentrations up to 30 wt% in PTMSP and Pebax 1074. The resulting sulfolene-doped PTMSP and Pebax 1074 films were mechanically stable over the additive concentration range explored. (For the PTMSP system, films were difficult to form beyond 30 wt% sulfolene content.)

The effect of 3-methyl sulfolene additive on CO_2 and H_2 permeation properties in PTMSP is shown in Figure 25. As sulfolene content increases from 0 to 30 wt%, the CO_2/H_2 selectivity of PTMSP increases from 2.3 to 6.5. This selectivity improvement, though, is accompanied by a permeability decrease of 24-fold for CO_2 and 100-fold for H_2. The presence of the large sulfolene filler particles apparently acts to hinder gas diffusion (and, hence, gas permeation) in PTMSP. However, the CO_2 permeability reduction is significantly less than that for H_2 due to sulfolene's affinity for CO_2, which keeps the CO_2 solubility (and, hence, its permeability) in the sulfolene-filled PTMSP fairly high still. The nearly 3-fold increase in acid-gas selectivity observed in a polymer with intrinsically low acid-gas selectivity, such as PTMSP, suggests that 3-methyl sulfolene and similar compounds may be useful for enhancing CO_2 and other acid gas separation properties of other polymer membrane materials.
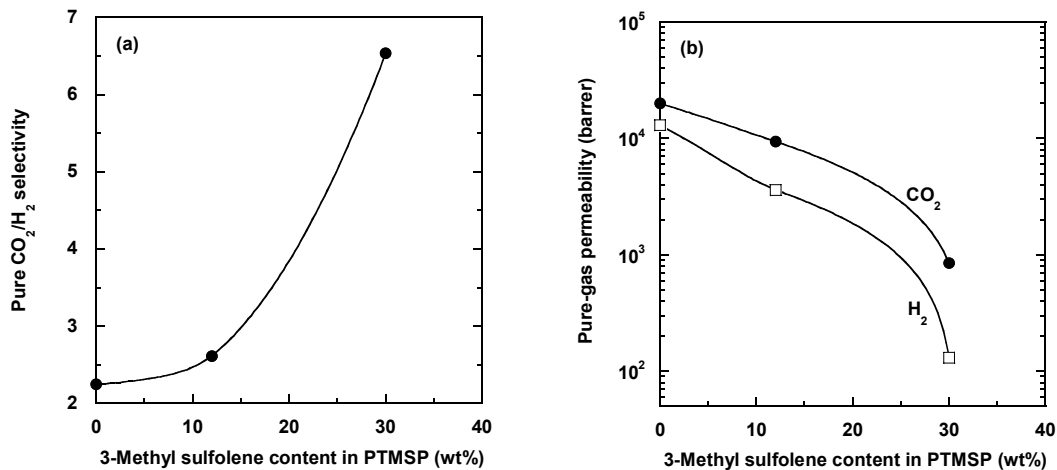
Figure 25. Effect of 3-methyl sulfolene concentration on (a) pure-gas CO_2/H_2 selectivity and (b) pure CO_2 and H_2 permeabilities of PTMSP at 21 °C. Feed pressure: 50 psig. Permeate pressure: 0 psig.

Consequently, we tried to extend the acid-gas adsorbent additive approach to a host polymer with higher intrinsic acid-gas selectivity. The next polymer matrix chosen was Pebax 1074, a rubbery polyether-polyamide block copolymer with a high CO_2/H_2 selectivity of ~8. Table 5 presents the pure- and mixed-gas CO_2 and H_2 permeation properties of a Pebax 1074 film filled with 10 and 30 wt% 3-methyl sulfolene. The permeation properties of Pebax filled with 10 wt% 3-methyl sulfolene are comparable to those of pure (unfilled) Pebax. This additive concentration, though, may have been too low to have any effect on the properties of the host Pebax polymer. Hence, a Pebax film with higher sulfolene content of 30 wt% was also prepared and tested; unfortunately, these data also suggest no clear effect on permeation properties relative to those in the unfilled polymer. Thus, dispersion of an acid-gas adsorbent such as 3-methyl sulfolene into a polymer matrix with a higher intrinsic acid-gas selectivity than that of PTMSP appears to show little, if any, improvement in the acid-gas separation properties of the base polymer.

Table 5. Pure- and Mixed-Gas CO_2 and H_2 Permeation Properties of Rubbery Pebax 1074 Polyether-Polyamide Block Copolymer Filled with 3-Methyl sulfolene at 21 °C

3-Methyl sulfolene content in Pebax 1074 (wt%)	Pure-gas permeability (barrer)		CO_2/H_2 selectivity	
	H_2	CO_2	Pure-gas	Mixed-gas
0 (*Unfilled polymer*)	6.8	57	8.4	8.4
10	6.8	62	9.1	8.0
30	7.3	62	8.5	—

Pure-gas tests: used. Feed pressure = 50 psig; Permeate pressure = 0 psig; Downstream He sweep

Mixed-gas tests: Binary feed of 25% CO_2 in H_2; Feed pressure = 50 psig; Permeate pressure = 0 psig; Downstream He sweep used; Stage-cut < 1%.

3.7 Other Rubbery Pebax Blend Films

In additional attempts to improve its CO_2 separation properties, the block copolymer Pebax 1074 was also physically blended with three other materials — fumed silica. polyethyleneimine [PEI], and a copolymer of PEI and poly(ethylene oxide) [PEO]. The permeation properties measured on these blend films are summarized in Table 6.

Nanoscale fumed silica was tried because Merkel et al. had recently discovered that that the addition of fumed silica to high-free-volume polymers can significantly enhance the solubility selectivity of such materials, thus increasing the overall gas selectivity for highly sorbing gases.[24] The first type of fumed silica added to the lower-free-volume Pebax was the hydrophobic silica, Cab-O-Sil® TS-530. Unfortunately, the resulting fumed-silica-filled Pebax film possessed weak mechanical properties and failed

during permeation testing. Incorporating a *hydrophilic* fumed silica into the relatively polar Pebax polymer may be more compatible and result in a mechanically more robust film; however, there was insufficient time to pursue this.

PEI is a viscous polymeric amine liquid possessing a very high concentration of amine groups. Because amine functional groups have a strong affinity for acidic and polar gases, PEI has been studied as an acid (polar)-gas scavenger and as a high-capacity adsorbent for CO_2.[75] As a result, films of Pebax blended with PEI-containing materials were also investigated. As shown in Table 2, films of Pebax mixed with pure PEI display a clear trend of decreasing gas permeability and decreasing CO_2/H_2 selectivity (i.e., increasing size selectivity for H_2 over CO_2) with increasing PEI content. This result suggests that any enhancement in CO_2/H_2 solubility selectivity afforded by the PEI domains is more than offset by the increase in diffusivity selectivity due to PEI addition. The situation is less clear for Pebax blended with a PEI-PEO copolymer. The incorporation of PEI-PEO copolymer at the low concentration of 22 wt% appears to reduce both gas permeability and CO_2/H_2 selectivity in a manner similar to pure PEI addition. At the higher 40 wt% PEI-PEO copolymer content in Pebax, the H_2 permeability increases to a value somewhat higher than that of pure Pebax. However, before the CO_2 permeability could be measured, this blend sample became defective upon exposure to CO_2. Examination of the sample indicates that, because of its much higher ether content, CO_2 had softened the blend film to the point where the film's mechanical strength was lost. On the basis of these results, blending Pebax with either PEI or PEI-PEO copolymer most probably does not improve acid-gas separation properties beyond those of base polymers already having moderately high acid-gas selectivity, such as Pebax or PEO.

Table 6. Pure CO_2 and H_2 Permeation Properties of Blend Films of Rubbery Pebax 1074 Polyether-Polyamide Block Copolymer and Various Additives at 21 °C

Additive blended into Pebax 1074	Pure-gas permeability (barrer)		Pure CO_2/H_2 selectivity
	H_2	CO_2	
0 (*Unfilled polymer*)	6.8	57	8.4
20 wt% TS-530 fumed silica	(*Failed*)[a]	(*Failed*)[a]	—
22 wt% PEI	2.8	21	7.5
40 wt% PEI	2.4	15	6.2
22 wt% PEI-PEO copolymer	4.9	35	7.1
40 wt% PEI-PEO copolymer	7.4	(*Failed*)[b]	—

ND ≡ Not determined

Pure-gas tests: Feed pressure = 50 psig; Permeate pressure = 0 psig; Downstream He sweep used.

[a] Film, though flexible, was mechanically weak and became defective upon exposure to feed gas.

[b] Film cracked around O-ring seal as it had substantially softened and weakened during CO_2 testing.

3.8 PTMSP Impregnated with PEI

In an attempt to study its separation characteristics in membrane form, the polymeric PEI liquid was loaded into PTMSP, a highly permeable, high-free-volume polymer with intrinsically low acid-gas selectivity (CO_2/H_2 selectivity ~ 2) and considered to be nanoporous in nature. In essence, by acting as a nanoporous support membrane, PTMSP may potentially be impregnated with PEI.

To check whether PEI improves the selectivity of PTMSP for CO_2, the gas permeation properties of a PTMSP membrane before and after PEI impregnation was evaluated with pure gases, including H_2 and CO_2. The PTMSP membrane was

impregnated with PEI (MW ~ 10,000) by immersing the PTMSP film in a low-viscosity solution of 10 wt% PEI in methanol for 36 h. Because PTMSP swells significantly in methanol at room temperature, PEI was expected to enter and fill the nanoporous PTMSP matrix. Upon removal from the impregnating solution, the PEI-loaded PTMSP was dried under vacuum at room temperature. The resulting PEI-loaded PTMSP membrane was fairly tacky.

The permeation results obtained on PTMSP before and after PEI loading are summarized in Figure 26 and Table 7. The pure, as-cast PTMSP membrane has high gas permeabilities that are in agreement with literature values. After treatment with less permeable PEI, all gas permeabilities in PTMSP are reduced. The CO_2/H_2 selectivity of PTMSP loaded with PEI, however, also decreases relative to that of plain PTMSP, even in a humidified feed environment (cf. Table 7). The PEI treatment appears to make PTMSP more size-selective for the smaller H_2 species. Two possible explanations may be (i) that the amount of PEI loaded into PTMSP was too low to improve CO_2 permeability or (ii) that PEI itself does not have high permeability for CO_2 despite the high CO_2 sorption capacity reported for this polyamine in literature.
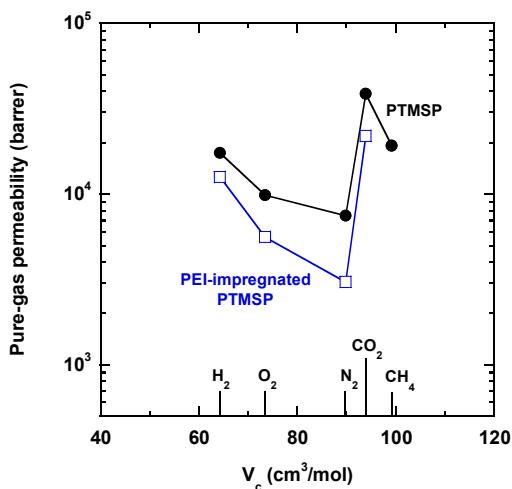
Figure 26. Pure-gas permeability in PTMSP at 22 ºC before and after impregnation with PEI as a function of gas permeant size (critical volume V_c). Feed pressure: 50 psig; Permeate pressure: 0 psig.

Table 7.　　Effect of PEI Impregnation on Pure H_2 and CO_2 Permeabilities of PTMSP in Dry and Moist Environments

Membrane	Dry or moist feed?	Pure-gas permeability (barrer)		Pure CO_2/H_2 selectivity
		H_2	CO_2	
Pure PTMSP	Dry	17,400	38,700	2.2
PEI-impregnated PTMSP	Dry	12,600	21,800	1.7
	Moist[a]	13,300	23,900	1.8
	Moist[a] (75 °C)	10,300	12,100	1.2

T = 22 °C, unless otherwise noted.

Feed pressure = 50 psig; Permeate pressure = 0 psig; No downstream sweep gas used.

[a]　Moist feed was obtained by passing dry feed gas through a bubbler filled with liquid water to saturate it with water vapor at the experimental temperature.

　　　Although the data above indicate that PEI does not seem to improve permeation of CO_2 over that of H_2 in PTMSP, PEI may still increase CO_2 uptake (solubility) in the PTMSP matrix. To determine whether PEI-impregnated PTMSP has higher CO_2 uptake than pure PTMSP, thermogravimetric (TGA) experiments in pure CO_2 and moist CO_2 environments were performed on a PTMSP loaded with 19 wt% PEI. For comparison, TGA tests were also conducted on control samples of pure PTMSP and pure PEI liquid. Mass uptake of TGA samples were systematically monitored in TGA environments of pure He, pure CO_2, moist He, and moist CO_2 at 75 °C and 1 atm. Pure He was used to create around the sample an inert, reference environment in which gas desorption from the sample can occur between different sorption cycles. Because He uptake in polymers and liquids is usually negligible relative to the uptake of penetrants such as CO_2 and moisture, sorption in the moist He atmosphere is essentially that of H_2O vapor. Table 8 presents the TGA results obtained on PEI-loaded PTMSP and compares them to those of

pure PTMSP and pure PEI. Buoyancy effects on the TGA results have been taken into account.

As shown in Table 8, impregnation of PTMSP with 19 wt% PEI does appear to increase the pure CO_2 uptake (affinity) by ~69% relative to that in pure PTMSP. More dramatic is the significantly higher H_2O vapor uptake (1.75 wt%) in the PEI-loaded PTMSP, compared to only 0.049 wt% in hydrophobic PTMSP alone. The pure PEI data confirm that this polyamine is strongly hydrophilic, sorbing a large amount of moisture. The CO2+water vapor uptake of 2.6 wt% observed for PEI-impregnated PTMSP suggests that the presence of water vapor may also enhance CO_2 uptake because this value is greater than the additive uptake of pure CO_2 and moisture (i.e., 0.64 wt% + 1.75 wt%). This synergistic effect of moisture on CO_2 sorption is not seen for PTMSP. In fact, PTMSP shows lower uptake of CO_2+water vapor than the sum of its individual CO_2 and moisture uptakes due to competitive sorption. Surprisingly, pure PEI by itself shows negligible CO_2 sorption in these TGA experiments. This observation conflicts with literature data showing that PEI should be able to sorb as much as 11 wt% CO_2 at 75 °C and 1 atm.[c] Possible explanations for this discrepancy may be that (i) the amine groups in PEI in pure polymeric liquid form were unavailable for CO_2 sorption because they were hidden and thus inaccessible to CO_2 or (ii) the active sorption sites in PEI were already saturated with CO_2 at the time of the experiment such that stronger desorption conditions would be required to completely outgas presorbed CO_2 from the sample before an experiment. In particular, the second reason (i.e., CO_2 is so strongly held by PEI that this gas cannot easily desorb at atmospheric pressure or at room or moderately warm temperatures), if true, may explain the lack of CO_2 transport enhancement in the gas permeation results shown in Table 7 and Figure 26. That is, CO_2 is not being easily desorbed (released) from the PEI-loaded membrane in permeation tests. This suggests that PEI, when dispersed on a substrate such as PTMSP, may be more useful as a sorbent for CO_2 (and H_2O vapor) than as a gas transport membrane

---

[c] See Footnote 2.

Table 8. Sorption Uptake Measured by TGA in Pure PTMSP, PEI-Impregnated PTMSP, and Pure PEI under Pure CO_2, Moist CO_2, and Moist He Atmospheres at 75 °C

Sorbent sample	Mass uptake[a] (wt%)		
	Pure CO_2	CO_2+H_2O vapor	H_2O vapor(+He)[b]
PTMSP	0.378	0.383	0.049
PTMSP+19 wt% PEI[c]	0.64	2.6	1.75
PEI (polymer liquid)[c]	*Negligible*	8.0	8.6

Sorption pressure = 1 atm
Gas flow rate = 35 cm^3/min for pure CO_2, moist CO_2, and moist He
Moist gas streams contain ~15 mol% water vapor in the gas of interest

[a] Mass uptake = (mass of gas sorbed/mass of sorbent) × 100

[b] Essentially H_2O vapor uptake because He sorption is negligible

[c] Data obtained at quasi-equilibrium state

3.9 Reverse-Selective, Rubbery, Cross-Linked Poly(ethylene oxide) [XL-PEO]

Polar ether linkages have a strong affinity for acid (and polar) gases such as CO_2 and H_2S. Thus, rubbery poly(ethylene oxide) [PEO] with its polar ether linkages was selected as a polymer to investigate for acid gas separation. The favorable interaction between polyether segments in this polymer and CO_2 is expected to enhance membrane permeability and selectivity for CO_2. However, conventional high-molecular-weight PEO polymer is not only difficult to form into useful membranes but also highly crystalline, leading to rather low intrinsic gas permeability (flux). By polymerizing PEO with UV light from low-molecular-weight poly(ethylene glycol)s, a rubbery PEO polymer that is wholly amorphous at room temperature and has a very high concentration of ether linkages can be formed. The amorphous PEO is also fairly strong because it undergoes chemical cross-linking during the photopolymerization process. Because it does not have crystallinity, the amorphous, cross-linked PEO [XL-PEO] possesses almost an order of magnitude higher gas permeability than conventional semicrystalline PEO.

3.9.1 Effect of Monomer Type

Rubbery XL-PEO films photopolymerized from monofunctional poly(ethylene glycol) monomers having two different end groups were evaluated for acid-gas separation performance with gas mixtures. One class of materials, designated as "XL-PEO (1)", was prepared using poly(ethylene glycol) acrylate [PEGA] monomer, which has a hydroxyl end group. The other class, labeled "XL-PEO (2)", was synthesized from poly(ethylene glycol) methyl ether acrylate [PEGMEA] monomer, which is methyl-terminated. Both XL-PEO classes used difunctional poly(ethylene glycol) diacrylate [PEGDA] as the cross-linking agent. All three components (PEGA, PEGMEA, PEGDA) have a high ethylene oxide content of 81-83%. A summary of the pure- and acid-gas separation properties obtained for XL-PEO (1) and XL-PEO (2) with pure gases and a H_2S-containing synthesis gas mixture is given in Table 9.

Table 9. Pure and Mixture Syngas Permeation Properties of XL-PEO (1) and XL-PEO (2) at 21-22 °C

Membrane	Pure-gas permeability (barrer)		Mixed-gas permeability (barrer)				Selectivity		
	H_2	CO_2	CO	H_2	CO_2	H_2S	Pure CO_2/H_2	Mixture CO_2/H_2	Mixture H_2S/H_2
XL-PEO (1) films[a]									
20% PEGA/20% PEGDA	12	72	2.0	15	97	510	6.0	6.5	34
10% PEGA/10% PEGDA	13	70	*ND*	15	92	470	5.4	6.1	31
0% PEGA/20% PEGDA	14	—	*ND*	14	83	520	—	5.9	37
0% PEGA/100% PEGDA	14	64	—	12	60	—	4.6	5.0	—
XL-PEO (2) film									
91% PEGMEA/9% PEGDA	48	410	11	50	360	2,500	8.5	7.2	50

ND ≡ Not determined because CO concentration was below GC resolution.

Pure-gas tests: Feed pressure = 50 psig; Permeate pressure = 0 psig; Downstream He sweep rate ~ 43 cm^3/min

Mixed-gas tests: Feed pressure =100 psig; Permeate pressure: 0 psig; Downstream He sweep rate ~ 43 cm^3/min; Stage-cut < 1%;

Feed mixture of 0.6% H_2S, 51% H_2, 11.7% CO_2, and 36.6% CO for all films, except 0% PEGA/100% PEGDA [XL-PEO (1)] and 91% PEGMEA/9% PEGDA [XL-PEO (2)];

Binary feed of 25% CO_2 and 75% H_2 for 0% PEGA/100% PEGDA [XL-PEO (1)];

Feed mixture of 1.0% H_2S, 35.7% H_2, 12.5% CO_2, and 50.8% CO for 91% PEGMEA/9% PEGDA [XL-PEO (2)]

[a]   Nomenclature is based on prepolymerization mixture composition. The remaining percentage balance in these films refers to the amount of water solvent used in prepolymerization mixtures.

By using the PEGMEA monomer with the bulkier methyl ether chain end group rather than the hydroxy-terminated PEGA monomer, XL-PEO (2) exhibits *both* higher gas permeability and higher acid-gas selectivity than the XL-PEO (1) films.   The

XL-PEO (2) film of composition 91% PEGMEA and 9% PEGDA has a permeability of 48 and 410 barrers for pure H_2 and CO_2, respectively, and a pure CO_2/H_2 selectivity of 8.5. Relative to that of the XL-PEO (1) films made from either solely PEGDA or a PEGA/PEGDA combination, XL-PEO (2) has a 6-fold higher pure CO_2 permeability and a 40-80% higher pure CO_2/H_2 selectivity. Additionally, XL-PEO (2) has an excellent mixture H_2S/H_2 selectivity of 50, the highest value that we have seen for a polymer. The measured mixture H_2S permeability of 2,500 barrers is also among the highest values obtained for polymers. The mixture CO_2/H_2 selectivity of XL-PEO (2) is ~15% lower than its measured pure-gas value mainly because of the lower CO_2 partial pressure driving force under the given mixture test conditions. More importantly, XL-PEO (2) achieves the higher permeability without sacrificing selectivity.

To better understand why permeability is higher in XL-PEO (2), the gas diffusivity and solubility components making up the overall gas permeability were decoupled. This analysis indicates that gas diffusion coefficients are substantially higher in XL-PEO (2) than in XL-PEO (1). The higher gas diffusivity in XL-PEO (2) is corroborated by its greater free volume, relative to that of XL-PEO (1), as determined by PALS, and is consistent with the larger free volume associated with the bulkier methyl ether end group in the PEGMEA monomer. The higher permeability will help significantly to reduce the membrane area required for a separation process. Of the reverse-selective polymers screened, XL-PEO (2) is a most promising membrane material for acid gas separation and was further studied with a binary CO_2/H_2 feed mixture.

As shown in Table 10, the feed pressure dependence of the mixture acid-gas separation properties of XL-PEO (2) was investigated with a binary CO_2/H_2 mixture. When the feed pressure was raised from 100 to 300 psig, the mixed-gas CO_2/H_2 selectivity rose from 7.8 to about 9.0 due to an increase in CO_2 partial pressure driving force and a small decrease in H_2 permeability (due to compressibility effect). The mixture CO_2 permeability remained essentially constant at 355-360 barrers over the given experimental pressure range.

To determine the potential effect of moisture on the acid-gas separation properties of XL-PEO (2), data obtained with a CO_2/H_2 feed saturated with water vapor at room temperature are also presented in Table 6. The presence of moisture in the feed appears to enhance the permeation of CO_2 in this membrane. Relative to the value obtained with a dry feed at the same pressure, the CO_2 permeability measured with a moist feed is 40% higher. The H_2 permeability, though, appears to be unaffected by the presence of water vapor at the given test conditions. As a result, the mixed-gas CO_2/H_2 selectivity increases from 7.8 (dry feed) to 12 (wet feed). Not too long after the experiment reached a pseudo-steady state, the XL-PEO (2) film failed mechanically. Moisture appears to weaken the polymer, making it more brittle and less elastic. In light of this failure, more moist feed tests should be conducted on XL-PEO to determine its longer-term mechanical stability in the presence of moisture. Optimization of the XL-PEO formulation would still be needed to make the material more robust for use under industrial conditions.

Table 10. Pure and Mixture Syngas Permeabilities in XL-PEO (2) at 22 °C

Feed type	Feed pressure (psig)	Gas permeability (barrer)		CO_2/H_2 selectivity
		H_2	CO_2	
Pure gas	50	48	410	8.5
Dry 2-component mixture[a]	100	46	360	7.8
	150	43	355	8.3
	200	38	355	9.3
	300	40	355	8.9
Wet 2-component mixture[b]	100	43	515	12

XL-PEO (2) film composition: 91% PEGMEA/9% PEGDA
Permeate pressure = 0 psig; Downstream He sweep rate ~ 43 cm^3/min

[a] Binary feed of 25% CO_2 in H_2; Stage-cut < 0.02%

[b] Humidified CO_2/H_2 feed mixture (25.12% CO_2 and 0.33% H_2O in H_2); Stage-cut < 0.05%

3.9.2 Effect of Ether Linkage Chemistry

Previous studies have suggested that acid-gas separation performance is closely linked to the concentration and availability of polar linkages in polymers.[76] To explore this influence of polar linkage chemistry on acid-gas permeation properties, novel cross-linked poly(propylene oxide) [XL-PPO] films of two different monomer/cross-linker compositions were prepared according to the UV photopolymerization process used to make for XL-PEO. One XL-PPO composition was 70 wt% poly(propylene glycol) methyl ether acrylate [PPGMEA] monomer and 30 wt% poly(propylene glycol) diacrylate [PPGDA] cross-linker; the second was 91 wt% PPGMEA and 9 wt% PPGDA. These XL-PPO films are mechanically more robust than XL-PEO samples. Compared to that of XL-PEO, the XL-PPO chemical structure has a methyl side group. To see the

effect of this methyl functionality on gas permeation behavior, the XL-PPO permeation results obtained are compared to those of XL-PEO in Table 11 and Figure 27.

The two XL-PPO films with different monomer/cross-linker ratios have essentially identical gas transport properties (cf. Table 11). Increasing the PPGMEA monomer content from 70 to 91 wt% in XL-PPO has negligible effect on H_2 permeability and only slightly increases CO_2 permeability. Compared to its PEO-based analog XL-PEO-91/9, XL-PPO-91/9 has ~11-16% lower CO_2 permeability and ~84% higher H_2 permeability. As a result, XL-PPO has CO_2/H_2 and H_2S/H_2 selectivities of only 4-5 and 12-13, respectively, significantly lower than those of the corresponding XL-PEO-91/9 film (CO_2/H_2 and H_2S/H_2 selectivities ~ 10 and 50, respectively).

Table 11. Acid-Gas Permeabilities and Selectivities Obtained for Dense XL-PPO and XL-PEO Films at 35 °C

Film sample	Feed type	Gas permeability (barrer)				Selectivity	
		CO	H_2	CO_2	H_2S	CO_2/H_2	H_2S/H_2
XL-PPO-70/30	Pure-gas *Before* syngas	—	81	350	—	4.3	—
	After syngas	—	83	350	—	4.2	—
	Mixed-gas	18	85	360	1,050	4.2	12
XL-PPO-91/9	Pure-gas *Before* syngas	—	84	400	—	4.8	—
	After syngas	—	83	395	—	4.8	—
	Mixed-gas	20	87	380	1,150	4.4	13
XL-PEO-91/9	Pure-gas *Before* syngas	—	45	450	—	10	—
	Mixed-gas	13	46	450	2,300	9.8	50

Film compositions: XL-PPO-70/30 ≡ 70 wt% PPGMEA/30 wt% PPGDA
XL-PPO-91/9 ≡ 91 wt% PPGMEA/9 wt% PPGDA
XL-PEO-91/9 ≡ 91 wt% PEGMEA/9 wt% PEGDA

Feed pressure = 50 psig (pure-gas) and 100 psig (mixed-gas)
Permeate pressure = 0 psig; Downstream He sweep rate = 43-44 cm^3/min

Syngas mixture used: 1.0% H_2S, 36% H_2, and 13% CO_2 in CO; Stage-cut < 1% in mixed-gas tests

The difference in acid-gas permeation behavior of XL-PPO and XL-PEO can be rationalized in terms of free volume and polarity of the polymer matrix. As shown in Table 12, the fractional free volume (FFV) of PPO-based materials is significantly higher than that of their PEO-based analogs. For example, for the 70/30 monomer/cross-linker composition, XL-PPO FFV is 48% higher than the FFV of the corresponding XL-PEO. The higher XL-PPO free volume is a consequence of the nonpolar pendant methyl group

attached to the polymer chain backbone. Because this methyl side group in XL-PPO is larger than the analogous hydrogen atom bonded to the XL-PEO backbone, it disrupts polymer chain packing efficiency and, thus, increases polymer free volume. In turn, increasing free volume tends to raise overall permeability of the polymer. As a result, XL-PPO has higher H_2 permeability than its XL-PEO counterpart. However, from the perspective of chemical polarity, PEO-based polymers possess a higher concentration of ether groups than those derived from PPO. This higher concentration of polar ether groups gives XL-PEO a greater affinity for acid gases such as CO_2 and, thus, compensates for the lower free volume (lower permeability) of XL-PEO by enhancing CO_2 solubility in this material. This "ether group" effect is manifested in XL-PEO having substantially higher acid-gas/H_2 selectivity than XL-PPO. Moreover, accessibility of ether linkages in XL-PPO to CO_2 may be lower possibly due to a "shielding" effect of the methyl side group in XL-PPO. Thus, for acid gas removal from syngas, XL-PEO still has the more desirable combination of selectivity and permeability relative to XL-PPO.
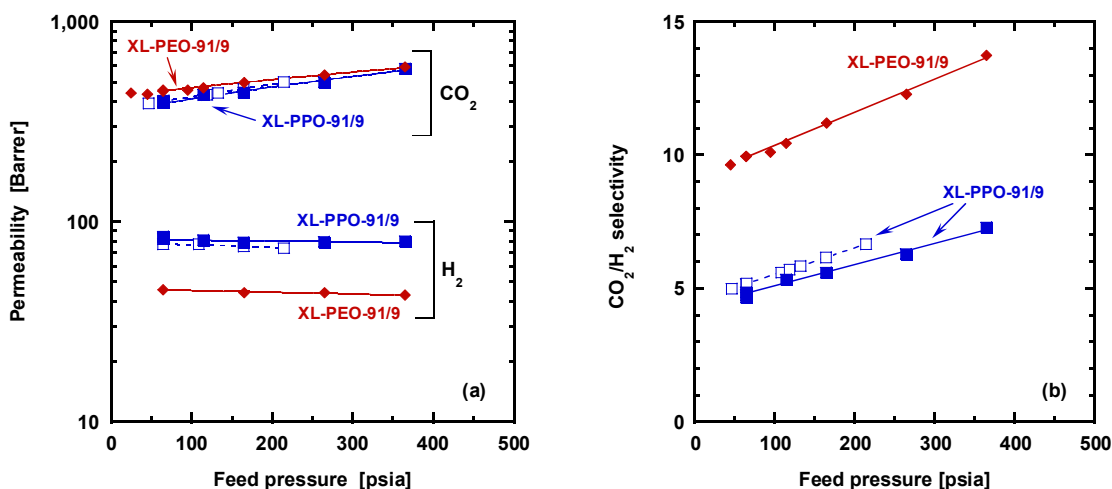
Figure 27. Comparison of (a) pure H_2 and CO_2 permeabilities and (b) pure CO_2/H_2 selectivity in XL-PPO and XL-PEO films as function of feed gas pressure at 35 °C. Film composition is 91 wt% PPGMEA/9 wt% PPGDA for XL-PPO and 91 wt% PEGMEA/9 wt% PEGDA for XL-PEO. Filled symbols represent data collected at RTI; open symbols are UT data. Permeate pressure: 0 psig.

Table 12. Density, Fractional Free Volume (FFV), and Gas Permeability of Various XL-PPO and XL-PEO Materials

Polymer	Prepolymer composition (wt%)		Density[a] (g/cm^3)	FFV[b]	Permeability[c] (barrer)	
	Monomer	Cross-linker			H$_2$	CO$_2$
XL-PEO-91/9	91 PEGMEA	9 PEGDA	1.140	0.136	46	520
XL-PEO-70/30	70 PEGMEA	30 PEGDA	1.155	0.128	31	320
XL-PPO-70/30	70 PPGMEA	30 PPGDA	1.075	0.190	77	360

[a] Polymer film density (ρ) was determined at 24 °C by hydrostatic weighing.

[b] Polymer FFV was estimated as $(V - V_o)/V$,[77] where $V = 1/\rho$ is the specific volume of the amorphous polymer at the temperature of interest and V_o is the specific occupied volume of the polymer at 0 K. Typically, V_o is computed as 1.3 times the van der Waals volume, which is determined by a group contribution method.

[c] Permeabilities were measured at 35 °C at feed pressure of 11 atm for H$_2$ and 14.6 atm for CO$_2$.

3.9.3 Rubbery XL-PEO/MgO Nanocomposite Membranes

A novel rubbery XL-PEO (70% PEGMEA/30% PEGDA) nanocomposite film containing 43 wt% MgO nanoparticles was prepared at UT and sent to RTI for evaluation. According to preliminary UT data, the MgO-filled XL-PEO nanocomposite should possess 3 times higher permeability than the unfilled XL-PEO without sacrificing the good CO$_2$/H$_2$ selectivity of 10-11 of the unfilled material. As shown in Table 13, RTI pure-gas results confirm that incorporation of nanoparticles can raise the gas permeability of the XL-PEO matrix. However, the 30-60% permeability improvement observed in RTI tests is significantly lower than that seen in preliminary UT experiments. After following up with UT, we realized that reproducibility of the properties of these nanocomposite films is an issue. For example, for a XL-PEO/MgO nanocomposite film from the same batch as the film tested at RTI, UT experiments indicated that this latest batch of nanocomposite films had a CO$_2$ permeability actually about 27% *lower* than neat

XL-PEO. At this time, we attribute the reproducibility of these XL-PEO nanocomposite membranes to variable quality control on the MgO nanoparticles.

Table 13. Pure H_2 and CO_2 Permeation Properties in XL-PEO/MgO Nanocomposite Films at 35 °C

Film	Permeability, Ba		CO_2/H_2 selectivity
	H_2	CO_2	
Unfilled XL-PEO (*UT data*)	32	350	11
XL-PEO + 43 wt% MgO (*RTI data on Batch #2 sample*)	51	460	9.0
XL-PEO + 43 wt% MgO (*Preliminary UT data on Batch #1 sample*)	91	940	10

XL-PEO composition: 70 wt% PEGMEA monomer with 30 wt% PEGDA cross-linker

Feed pressure = 51 psig; Permeate pressure = 0 psig; Downstream He sweep rate ~ 43 cm^3/min

4. Conclusions

This research has resulted in two significant findings regarding nanocomposites: First, addition of MgO nanoparticles to PTMSP membranes significantly changes gas transport properties relative to those of the native polymer. The diffusion coefficients for gases considered in this research increase significantly at MgO loadings in excess of 19 volume percent. This increase in diffusion coefficients is attributed to the creation of additional void space in the membrane as MgO loading increases. The solubility of MgO filled PTMSP also has a strong dependence on particle loading, although the behavior of CO_2 and N_2 solubilities at high loadings is not yet understood. Due to the effect of MgO nanoparticles on diffusion and solubility, the light gas permeability increases with particle loading. Permeabilities in the 100,000 – 1,000,000 barrer range are observed, and the materials maintain some degree of reverse selective properties.

Second, MgO nanoparticles interact strongly with the trimethylsilyl group of PTMSP. This interaction facilitates dispersion of the nanoparticles in the polymer, and it contributes to the formation of nanocomposites with extremely high MgO loadings (*i.e.,* 70 nominal volume percent MgO). What is more, under certain circumstances, the interaction results in a desilylation reaction not only for polymers but for analogous small organic molecules.

The addition of other CO_2 selective materials reduced PTMSP and Pebax CO_2 permeability. Addition of 3-methyl sulfolene has a detrimental effect on permeability in PTMSP but not in Pebax. Addition of PEI to Pebax and PTMSP resulted in similar decreases in light gas permeability with increased loadings. While 3-methyl sulfolene did as much as triple CO_2/H_2 selectivity, neither of these two additive materials appreciably altered the CO_2/H_2 selectivity of the Pebax.

The gas transport properties of XLPEO were dependent on the monomers used to make the polymer. By changing the hydroxyl end groups of poly(ethylene glycol) to methyl groups the permeability increased significantly for all test gases. The ether linkages also influenced the permeability properties of light gases, (*e.g.*, CO_2 permeability in XLPEO was 18% higher than the comparable XLPPO membrane). Also, addition of nanoparticles to XLPEO increased the permeability of test gases without a significant loss of light gas selectivity.

5. Publications Resulting from the Grant

Wang, X. Y.; Raharjo, R. D.; Lee, H. J.; Freeman, B. D.; Sanchez, I.C., Molecular simulation and experimental study of substituted polyacetylenes: fractional free volume, cavity size distributions and diffusion coefficients, In preparation.

Raharjo, R. D.; Lee, H. J.; Freeman, B. D.; Sakaguchi, T.; Masuda, T.; Pure Gas and Vapor Permeation Properties of Poly[1-phenyl-2-[*p*-(trimethylsilyl)phenyl]acetylene] (PTMSDPA) and its Desilylated Analog, Poly[diphenylacetylene] (PDPA), Submitted to Polymer.

Lin, H.; Freeman, B.D,; Permeation and Diffusion, A chapter for Springer-Handbook of Materials Measurement Methods, In Press.

Lin, H.; Freeman, B.D,; Kalakkunnath, S.; Kalika, D.S., Re-Evaluating the Effect of Crosslinking on Gas Permeability in Crosslinked Poly(ethylene glycol diacrylates), In preparation.

Lin, H.; Freeman, B.D,; Gas Solubility in Crosslinked Poly(ethylene glycol Acrylates), In preparation.

Lin, H.; Freeman, B.D,; Gas Permeation and Diffusion in Crosslinked Poly(ethylene glycol Acrylates), In preparation.

Andrady, A. L., Merkel, T. C., and Toy, L. G., Effect of Particle Size on Gas Permeability of Filled Superglassy Polymers, *Macromolecules*, **37**, 4329 (2004).

Merkel, T. C., Toy, L. G., Andrady, A. L., Gracz, H., and Stejskal, E. O., Investigation of Enhanced Free Volume in Nanosilica-Filled Poly(1-trimethylsilyl-1-propyne) by ^{129}Xe NMR Spectroscopy, *Macromolecules*, **36**, 353 (2003).

6. References

(1)   Baker, R. W. Membrane Technology and Applications; McGraw-Hill: New York, 2000.
(2)   Kohl, A.; Nielsen, R. Gas Purification, 5th ed.; Gulf Publishing Company: Houston, 1997.
(3)   MSDS Monoethanolamine, **2004**, Equistar, pp 1-9
(4)   Dresselhaus, M. Basic Research Needs for the Hydrogen Economy; Argonne National Laboratory, 2003; Vol. http://www.sc.doe.gov/bes/hydrogen.pdf.
(5)   Joensen, F.; Rostrup-Nielsen, J. R., Conversion of Hydrocarbons and Alcohols for Fuel Cells, *Journal of Power Sources* **2002**, *105*, 195-201.
(6)   Ghosal, K.; Freeman, B. D., Gas Separation Using Polymer Membranes: An Overview., *Polymer Advanced Technology* **1994**, *5*, 673-697.
(7)   Koros, W. J., "Gas Separation" in Membrane Separation Systems - A Research and Development Needs Assessment, **1990**, US Department of Energy, Publication # DOE/ER/30133-H1, pp 3-4
(8)   Reid, R. C.; Prausnitz, J. M.; Poling, B. E. The Properties of Gases and Liquids, 4th ed.; McGraw-Hill: New York, 1987.
(9)   Merkel, T. C.; Bondar, V.; Nagai, K.; Freeman, B. D., Sorption and Transport of Hydrocarbon and Perfluorocarbon Gases in Poly(1-trimethylsilyl-1-propyne), *Journal of Polymer Science Part B: Polymer Physics* **1999**, *38*, 273-296.
(10)   Merkel, T. C.; He, Z.; Pinnau, I.; Freeman, B. D.; Hill, A. J.; Meakin, P., Effect of Nanoparticles on Gas Sorption and Transport in Poly(1-trimethylsilyl-1-propyne), *Macromolecules* **2003**, *36*, 8406-8414.
(11)   Lin, H.; Freeman, B. D., Gas Solubility, Diffusivity and Permeability in Poly(ethylene oxide), *Journal of Membrane Science* **2004**, *239*, 105-117.
(12)   Bondar, V.; Freeman, B. D.; Pinnau, I., Gas Sorption and Characterization of Poly(ether-b-amide) Segmented Block Copolymers, *Journal of Polymer Science, Part B: Polymer Physics* **1999**, *37*, 2463-2475.
(13)   Freund, H.-J.; Roberts, M. W., Surface Chemistry of Carbon Dioxide, *Surface Science Reports* **1996**, *25*, 225-273.
(14)   Stark, J. V.; Park, D. G.; Lagadic, I.; Klabunde, K. J., Nanoscale Metal Oxide Particles/Clusters as Chemical Reagents. Unique Surface Chemistry on Magnesium Oxide As Shown by Enhanced Adsorption of Acid Gases (Sulfur Dioxide and Carbon Dioxide) and Pressure Dependence, *Chemistry of Materials* **1996**, *8*, 1904-1912.
(15)   Freeman, B. D.; Pinnau, I. *Polymeric Materials for Gas Separations*, In Polymer Membranes for Gas and Vapor Separation, ACS Symposium Series; Freeman, B. D.; Pinnau, I., Eds.: Washington, D.C., 1999; Vol. 733, pp 1-27.
(16)   Barrer, R. M. Diffusion in Polymers; Academic Press: New York, 1968.
(17)   Maxwell, C. Treatise on Electricity and Magnetism; Oxford University Press: London, 1873; Vol. 1.
(18)   Barrer, R. M.; Barrie, J. A.; Rogers, M. G., Heterogenous Membranes: Diffusion in Filled Rubber, *Journal of Polymer Science, Part A: Polymer Chemistry* **1963**, *1*, 2565-2586.
(19)   Merkel, T. C.; Freeman, B. D.; Spontak, R. J.; He, Z.; Pinnau, I.; Meakin, P.; Hill, A. J., Sorption, Transport, and Structural Evidence for Enhanced Free Volume in Poly(4-methyl-2-pentyne)/ Fumed Silica Nanocomposite Membranes, *Chemistry of Materials* **2003**, *15*, 109-123.
(20)   Polotskaya, G. A.; Andreeva, D. V.; El'yashevich, G. K., Investigation of Gas Diffusion Through Films of Fullerene-containing Poly(phenylene oxide), *Technical Physics Letters* **1999**, *25*, 555-557.

(21)   Chung, T.-S.; Chan, S. S.; Wang, R.; Lu, Z.; He, C., Characterization of Permeability and Sorption in Matrimid/C_{60} Mixed Matrix Membranes, *Journal of Membrane Science* **2003**, *211*, 91-99.

(22)   Higuchi, A.; Yoshida, T.; Imizu, T.; Mizoguchi, K.; He, Z.; Pinnau, I.; Nagai, K.; Freeman, B. D., Gas Permeation of Fullerene-dispersed Poly(1-trimethylsilyl-1-propyne) Membranes, *Journal of Polymer Science, Part B: Polymer Physics* **2000**, *38*, 1749-1755.

(23)   Higuchi, A.; Agatsuma, T.; Uemiya, S.; Kojima, T.; Mizoguchi, K.; Pinnau, I.; Nagai, K.; Freeman, B. D., Preparation and Gas Permeation of Immobilized Fullerene Membranes, *Journal of Applied Polymer Science* **2000**, *7*, 529-537.

(24)   Merkel, T. C.; Freeman, B. D.; Spontak, R. J.; He, Z.; Pinnau, I.; Meakin, P.; Hill, A. J., Ultrapermeable, Reverse-Selective Nanocomposite Membranes, *Science* **2002**, *296*, 519-522.

(25)   He, Z.; Pinnau, I.; Morisato, A., Nanostructured Poly(4-methyl-2-pentyne)/silica Hybrid Membranes for Gas Separation, *Desalination* **2002**, *146*, 11-15.

(26)   Barsema, J. N.; Balster, J.; Jordan, V.; van der Vegt, N. F. A.; Wessling, M., Functionalized Carbon Molecular Sieve Membranes Containing Ag-nanoparticles, *Journal of Membrane Science* **2003**, *219*, 47-57.

(27)   van Amerongen, G. J., Diffusion in Elastomers, *Rubber Chemical Technology* **1964**, *37*, 1065-1153.

(28)   Merkel, T. C.; Bondar, V.; Nagai, K.; Freeman, B. D.; Pinnau, I., Gas Sorption, Diffusion, and Permeation in Poly(dimethylsiloxane), *Journal of Polymer Science Part B: Polymer Physics* **2000**, *38*, 415-434.

(29)   Lin, H.; Freeman, B. D.; Toy, L. G.; Bondar, V.; Gupta, R. P.; Pas, S.; Hill, A. J. In *228th ACS National Meeting*: Philidelphia, PA, United States, 2004.

(30)   Hirayama, Y.; Kase, Y.; Tanihara, N.; Sumiyama, Y.; Kusuki, Y.; Haraya, K., Permeation Properties to CO_2 and N_2 of Poly(ethylene oxide)-containing and Crosslicked Polymer Films., *Journal of Membrane Science* **1999**, *160*, 87-99.

(31)   Merkel, T. C.; Gupta, R. P.; Turk, B. S.; Freeman, B. D., Mixed-gas Permeation of Syngas Components in Poly(dimethylsiloxane) and Poly(1-trimethylsilyl-1-propyne) at Elevated Temperatures, *Journal of Membrane Science* **2001**, *191*, 85-94.

(32)   Nagai, K.; Masuda, T.; Nakagawa, T.; Freeman, B. D.; Pinnau, I., Poly[1-(trimethylsilyl)-1-propyne] and Related Polymers: Synthesis, Properties and Functions, *Prog. Polymer Science* **2001**, *26*, 721-798.

(33)   Auroux, A.; Gervasini, A., Macrocalorimetric Study of the Acidity and Basicitiy of Metal Oxide Surfaces, *Journal of Physical Chemistry* **1990**, *94*, 6371-6379.

(34)   Backx, C.; De Groot, C. P. M.; Biloen; Sachtler, W. M. H., Interaction of O_2, CO_2, CO, C_2H_4, and C_2H_4O with Ag(100), *Surface Science* **1983**, *128*, 81-103.

(35)   Erdohelyi, A.; Anneser, E.; Bauer, T.; Stephan, K.; Borgmann, D.; Wedler, G., Interaction of Carbon Dioxide and Oxygen on Iron Films at 273 K, *Surface Science* **1990**, 57-66.

(36)   Rollason, R. J.; Plane, J. M. C., A Kinetic Study of the Reactions of MgO with H_2O, CO_2, and O_2: Implications for Magnesium Chemistry in the Mesosphere, *Physical Chemistry Chemical Physics* **2001**, *3*, 4733-4740.

(37)   Zecchina, A.; Lofthouse, M. G.; Stone, F. S., Reflectance Spectra of Surface States in Magnesium Oxide and Calcium Oxide, *Journal of the Chemical Society, Faraday Transactions 1: Physical Chemistry in Condensed Phases* **1975**, *71*, 1476-1490.

(38)   Zecchina, A.; Stone, F. S., Reflectance Spectra of Surface States in Strontium Oxide and Barium Oxide, *Journal of the Chemical Society, Faraday Transactions 1: Physical Chemistry in Condensed Phases* **1976**, *72*, 2364-2374.

(39)   Horiuchi, T.; Hiroaki, H.; Takehisa, F.; Kubo, Y.; Horio, M.; Suzuki, K.; Mori, T., Effect of Added Basic Metal Oxides on CO_2 Adsorption on Alumnia at Elevated Temperatures, *Applied Catalysis A: General* **1998**, *167*, 195-202.

(40)   Ferrari, A. M.; Soave, R.; D'Ercole, A.; Pisani, C.; Giamello, E.; Pacchioni, G., Theoretical Characterization of Charge-Transfer Reactions Between N_2 and O_2 Molecules and Paramagnetic Oxygen Vacancies on the MgO Surface, *Surface Science* **2001**, 83-97.

(41)   Koper, O. B.; Lagadic, I.; Volodin, A. M.; Klabunde, K. J., Alkaline-Earth Oxide Nanoparticles Obtained by Aerogel Methods. Characterization and Rational for Unexpectedly High Surface Chemical Reactivities, *Chemistry of Materials* **1997**, *9*, 2468-2480.

(42)   Meixner, D. L.; Arthur, D. A.; George, S. M., Kinetics of Desorption, Adsorption, and Surface Diffusion of CO_2 on MgO(100), *Surface Science* **1992**, *261*, 141-154.

(43)   Pacchioni, G., Physisorbed and Chemisorbed CO_2 at Surface and Step Sites of MgO(100) Surface, *Surface Science* **1993**, *281*, 207-219.

(44)   Coluccia, S.; Boccuzzi, F.; Ghiotti, G.; Morterra, C., Infrared Study of Hydrogen Adsorption on MgO, CaO, and SrO, *Journal of the Chemical Society, Faraday Transactions 1: Physical Chemistry in Condensed Phases* **1982**, *78*, 2111-2119.

(45)   Pacchioni, G.; Ricart, J. M.; Illas, F., Ab Initio Cluster Model Calculations of Chemisorption of CO_2 and SO_2 Probe Molecules on MgO and CaO (100) surfaces. A Theorhetical Measure of Oxide Basicity, *Journal of the American Chemical Society* **1994**, *116*, 10152-10158.

(46)   Rasmussen, P. B.; Kazuta, M.; Chorkendorff, I., Synthesis of Methanol From a Mixture of H_2 and CO_2 on Cu (100), *Surface Science* **1994**, *318*, 267-280.

(47)   Fujita, S.-I.; Takezawa, N., Difference in the Selectivity of CO and CO_2 Methanation Reactions, *Chemical Engineering Journal* **1997**, *68*, 63-68.

(48)   Yu, Y.; Guo, Q.; Liu, S.; Wang, E., Partial Dissociation of Water on a MgO(100) Film, *Physical Review B* **2003**, *68*, 1-4.

(49)   Beruto, D. T.; Botter, R., Liquid-like H_2O Adsorption Layers to Catalyze the $Ca(OH)_2/CO_2$ Solid-gas Reaction and to Form a Non-protective Solid Product Layer at 20^oC, *Journal of the European Ceramic Society* **2000**, *20*, 497-503.

(50)   Xu, M.; Iglesia, E., Readsorption and Adsorption-Assisted Desorption of CO_2 on Basic Solids, *Journal of Physical Chemistry Pary B* **1998**, *102*, 961-966.

(51)   Onishi, H.; Egawa, C.; Aruga, T.; Iwasawa, Y., Adsorption of Sodium Atoms and Oxygen-containing Molecules on Magnesia(100) and (111) Surfaces, *Surface Science* **1987**, *191*, 479.

(52)   Bowker, M.; Barteau, M. A.; Madix, R. J., Oxygen Induced Adsorption and Reaction of H_2, H_2O, CO, and CO_2 on Single Crystal Ag(100), *Surface Science* **1980**, *92*, 528-548.

(53)   Outka, D. A.; Madix, R. J., The Oxidation of Carbon Monoxide on the Au(110) Surface, *Surface Science* **1987**, *179*, 351-360.

(54)   MSDS of $Mg(OH)_2$, **2004**, Sigma Aldrich,

(55)   Nanoactive Magnesium Oxide Plus: Technical Sheet, **2004**, Nanoscale,

(56)   Stern, S. A.; Gareis, P. J.; Sinclair, T. F.; Mohr, P. H., Performance of a Versatile Variable-volume Permeability Cell. Comparison of Gas Permeability Measurements by the Variable-volume and Variable-pressure Methods., *Journal of Applied Polymer Science* **1963**, *7*, 2035-2051.

(57)   McDowell, C. C.; Coker, D. T.; Freeman, B. D., An Automated Spring Balance for Kinetic Gravimetric Sorption of Gases and Vapors in Polymers, *Review of Scientific Instruments* **1998**, *69*, 2510-2513.

(58)   Pauling. <u>The Nature of the Chemical Bond</u>; Cornell University Press: Ithaca, NY, 1940.

(59)   Roberts, J. D.; McElhill, E. A.; Armstrong, R., The Electrical Effect of the Trimethylsilyl Group, *Journal of the American Chemical Society* **1949**, *71*, 2923-2926.

(60)   Soffer, H.; De Vries, T., Dipole Moments of Aromatic Derivatives of Trimethylsilane, *Journal of American Chemical Society* **1951**, *73*, 5817-5819.

(61)   Radovanovic, E.; Carone, E. J.; Goncalves, M. C., Comparative AFM and TEM Investigation of the Morphology of Nylon6-rubber Blends, *Polymer Testing* **2004**, 231-237.

(62)   Jeszka, J. K.; Tracz, A.; Wostek, D.; Boiteux, G.; Kryszewski, M., Preparation of Organic Metal Nanocrystals in Polymer Matrix, *Synthetic Metals* **2000**, 165-168.

(63)   Khanna, S. K.; Ranganathan, P.; Yedla, S. B.; Winter, R. M.; Paruchuri, K., Investigation of Nanomechanical Properties of the Interphase in a Glass Fiber Reinforced Polyester Composite Using Nanoindentation, *Journal of Engineering Materials and Technology* **2003**, *125*, 90-96.

(64)   Kirsch, S.; Pfau, A.; Stubbs, J.; Sundberg, D., Control of Particle Morphology and Film Structures of Carboxylated Poly(*n*-butylacrylate)/poly-(methyl-methacrylate) Composite Latex Particles, *Colloids and Surfaces A: Physiochemical and Engineering Aspects* **2001**, *183-185*, 725-737.

(65)   Oscillatory Modes in AFM, **2004**, National Physics Laboratory,

(66)   Vu, D. Q.; Koros, W. J.; Miller, S. J., Mixed Matrix Membranes Usinag Carbon Molecular Sieves I. Preparation and Experimental Results, *Journal of Membrane Science* **2003**, *211*, 311-334.

(67)   Pierce, A. E. <u>Silylation of Organic Compounds</u>; Pierce Chemical Company: Rockford, Illinois, 1968.

(68)   Utamapanya, S.; Klabunde, K. J.; Schlup, J. R., Nanoscale Metal Oxide Particles/Clusters as Chemical Reagents. Synthesis and Properties of Ultrahigh Surface Area Magnesium Hydroxide and Magnesium Oxide, *Chemical Materials* **1991**, *3*, 175-181.

(69)   Rethwisch, D. G.; Dumesic, J. A., Effect of Metal-Oxygen Bond Strength on Properties of Oxides. 1. Infrared Spectroscopy of Adsorbed CO and CO_2, *Langmuir* **1986**, *2*, 73-79.

(70)   Philipp, R.; Fujimoto, K., FTIR Spectroscopic Study of CO_2 Adsorption/Desorption on MgO/CaO Catalysts, *Journal of Physical Chemistry* **1992**, 9035-9038.

(71)   Colthup, N. B.; Daly, L. H.; Wiberly, S. E. <u>Introduction to Infrared and Raman Spectroscopy</u>, 2nd ed.; Academic Press: New York, 1975.

(72)   Sherill, A. B.; Barteau, M. A., Oligomerization of Trimethylsilyl Acetylene to Form Large Molecules on Reduced Surfaces of TiO_2 (001), *Journal of Molecular Catalysis A: Chemical* **2002**, *184*, 301-310.

(73)   Paparazzo, E.; Fanfoni, M.; Severini, E., Studies on the Structure of the SiO_x/SiO_2 Interface, *Applied Surface Science* **1992**, *56-58*, 866-872.

(74)   Mulder, M. <u>Basic Principles of Membrane Technology</u>; Kluwer Academic Press: Boston, 1996.

(75)   Xu, X.; Song, C.; Andersen, J. M.; Miller, B. G.; Scaroni, A. W., Novel Polyethylenimine-Modified Mesoporous Molecular Sieve of MCM-41 Type as High-Capacity Adsorbent for CO_2 Capture, *Energy and Fuels* **2002**, *16*, 1463-1469.

(76)   Bondar, V.; Freeman, B. D.; Pinnau, I., Proceedings of the American Chemical Society, Divison of Polymeric Materials: Science and Engineering, **1997**, *77*, 311-312.

(77)   van Krevelen, D. W. Properties of Polymers; Elsevier: Amsterdam, 1990.